JCI insight

RESEARCH ARTICLE

Improved efficacy of a next-generation ERT in murine Pompe disease

Su Xu,[1] Yi Lun,[1] Michelle Frascella,[1] Anadina Garcia,[1] Rebecca Soska,[1] Anju Nair,[1] Abdul S. Ponery,[1] Adriane Schilling,[1] Jessie Feng,[1] Steven Tuske,[1] Maria Cecilia Della Valle,[1] José A. Martina,[2] Evelyn Ralston,[3] Russell Gotschall,[1] Kenneth J. Valenzano,[1] Rosa Puertollano,[2] Hung V. Do,[1] Nina Raben,[2] and Richie Khanna[1]

[1]Amicus Therapeutics, Cranbury, New Jersey, USA. [2]Laboratory of Protein Trafficking and Organelle Biology, Cell Biology and Physiology Center, National Heart, Lung and Blood Institute, NIH, Bethesda, Maryland, USA. [3]Light Imaging Section, National Institute of Arthritis and Musculoskeletal and Skin Diseases, NIH, Bethesda, Maryland, USA.

Pompe disease is a rare inherited disorder of lysosomal glycogen metabolism due to acid α-glucosidase (GAA) deficiency. Enzyme replacement therapy (ERT) using alglucosidase alfa, a recombinant human GAA (rhGAA), is the only approved treatment for Pompe disease. Although alglucosidase alfa has provided clinical benefits, its poor targeting to key disease-relevant skeletal muscles results in suboptimal efficacy. We are developing an rhGAA, ATB200 (Amicus proprietary rhGAA), with high levels of mannose-6-phosphate that are required for efficient cellular uptake and lysosomal trafficking. When administered in combination with the pharmacological chaperone AT2221 (miglustat), which stabilizes the enzyme and improves its pharmacokinetic properties, ATB200/AT2221 was substantially more potent than alglucosidase alfa in a mouse model of Pompe disease. The new investigational therapy is more effective at reversing the primary abnormality – intralysosomal glycogen accumulation – in multiple muscles. Furthermore, unlike the current standard of care, ATB200/AT2221 dramatically reduces autophagic buildup, a major secondary defect in the diseased muscles. The reversal of lysosomal and autophagic pathologies leads to improved muscle function. These data demonstrate the superiority of ATB200/AT2221 over the currently approved ERT in the murine model.

Introduction

Pompe disease, also known as acid maltase deficiency or glycogen storage disease type II (GSD II), is a rare and often fatal muscle disease caused by mutations in the *GAA* gene, which encodes the lysosomal hydrolase acid α-glucosidase (GAA) (1, 2). Deficiency of GAA results in accumulation of glycogen within lysosomes, leading to progressive disruption of cellular function, especially in smooth, cardiac, and skeletal muscle cells. If left untreated, patients with infantile-onset Pompe disease (IOPD) usually die by 1 year of age, primarily due to cardiorespiratory failure (3, 4). In comparison, late-onset Pompe disease (LOPD) manifests as a much broader spectrum of symptoms, age of onset, and severity largely depending on residual GAA activity levels (1, 5). Progressive muscle weakness and loss of motor function are typical characteristics of the disease in affected individuals. Respiratory muscle weakness, particularly of the diaphragm, is the leading cause of death in LOPD (2, 6).

To date, enzyme replacement therapy (ERT) with intravenous (i.v.) administration of recombinant human GAA (rhGAA), alglucosidase alfa (Myozyme and Lumizyme, Sanofi Genzyme), is the only approved treatment for Pompe disease. Although alglucosidase alfa has provided benefits, particularly in IOPD (7–12), the clinical outcomes vary markedly among patients, and the consensus is that the therapy does not reverse, but rather attenuates disease progression, and that significant unmet medical needs remain (13–17). This is primarily due to the fact that skeletal muscle, one of the main affected tissues, responds poorly to current therapy (reviewed in ref. 18). Furthermore, the majority of IOPD patients who survive infancy due to reversal of cardiac abnormalities develop a slowly progressive myopathy (16, 19), even when treated neonatally (16, 19, 20). Autophagic defect, a major contributor to muscle damage (21, 22), persists despite ERT (16, 23, 24). Another limitation is the immune response to alglucosidase alfa, especially in cross-reactive immunologic material–negative infants (25). High antibody titers have also been reported in adults (26, 27) but their effect does not seem to interfere with the ERT efficacy in the majority of patients (28).

Authorship note: SX and YL contributed equally to this work.

Conflict of interest: SX, YL, MF, AG, RS, AN, ASP, AS, JF, ST, MCDV, RG, KJV, HVD, and RK are employees and shareholders of Amicus Therapeutics.

Submitted: October 5, 2018
Accepted: January 17, 2019
Published: March 7, 2019

Reference information:
JCI Insight. 2019;4(5):e125358.
https://doi.org/10.1172/jci.insight.125358.

A major drawback of alglucosidase alfa is its poor targeting to skeletal muscles. The uptake of rhGAA into cells and its subsequent delivery to lysosomes are mediated by the cation-independent mannose-6-phosphate receptor (CI-MPR) (29, 30). The relatively low abundance of CI-MPR at the surface of skeletal muscle (31) and the lower blood flow in this tissue are limiting factors; the situation is further exacerbated by the poor affinity of alglucosidase alfa glycans for CI-MPR due to their low mannose-6-phosphate (M6P) content (32). Several attempts have been made to improve the delivery of rhGAA to skeletal muscle by increasing its affinity for CI-MPR. One involves the chemical modification of glycan structures of rhGAA (32, 33); the clinical efficacy and safety of this investigational therapy (avalglucosidase alfa, also called neo-GAA) is currently being studied in patients with Pompe disease (NCT02782741). Another approach explored glycosylation-independent lysosomal targeting (GILT) using a novel chimeric enzyme in which rhGAA was fused with a portion of insulin-like growth factor 2 (34); however, development of this drug was terminated in phase 3 clinical studies (NCT01924845).

We have developed a proprietary cell line that yields what we believe is a novel rhGAA, ATB200 (Amicus proprietary rhGAA). ATB200 has substantially higher M6P content than alglucosidase alfa, including both mono- and bis-phosphorylated forms, with the latter having an even higher affinity for the CI-MPR (35) for uptake in muscle. In an in vitro assay, ATB200 demonstrated improved uptake into myoblasts compared with alglucosidase alfa (R. Gotschall, unpublished observations). We are developing ATB200 as a next-generation therapy for Pompe disease by coadministering it with the small-molecule pharmacological chaperone (PC) AT2221 (miglustat, *N*-butyl-deoxynojirimycin [NB-DNJ], active ingredient of Zavesca [Actelion Pharmaceuticals], approved for the treatment of type I Gaucher and Niemann-Pick type C diseases). The combination therapy (ATB200/AT2221) is based on the principle that selective binding of the PC stabilizes the conformation of the enzyme, thus improving its pharmacological properties (36–38).

The concept of coadministration of AT2221 with rhGAA for Pompe disease comes from previous studies showing that miglustat (active ingredient of AT2221) improved stability of rhGAA and its uptake in Pompe disease fibroblasts and in muscle of *Gaa*-knockout (*Gaa*-KO) mice (39). Enhanced rhGAA activity in blood in the presence of the PC was also observed in ERT-treated patients with Pompe disease (37). In addition, improved tolerability and alleviation of infusion-associated reactions were reported following coadministration of miglustat and rhGAA (Barry Byrne, unpublished observations). These data highlight the potential advantages of coadministration of a PC on the pharmacokinetics (PK), safety, and tolerability of the replacement enzyme. Therefore, we coadministered ATB200 with AT2221 to add the benefits of stability and tolerability to a highly phosphorylated enzyme with better muscle-targeting properties. Here, we present the results of extensive preclinical studies of the effects of ATB200/AT2221 on enzyme uptake, muscle pathology, and muscle function as compared with alglucosidase alfa.

Results

AT2221 stabilizes ATB200, preventing its denaturation and loss of activity. AT2221 is a small-molecule iminosugar that is structurally similar to the terminal glucose of glycogen (40), the natural substrate of GAA (Figure 1A). The effect of AT2221 binding on the stability of ATB200 was evaluated in vitro and in vivo. In a fluorescence-based thermal denaturation assay, ATB200 was significantly less stable at pH 7.4 (melting temperature [T_m] = 51.2°C) than at the acidic pH 5.2 (T_m = 67.2°C), which closely mimics the pH of the lysosome (Figure 1B). Importantly, AT2221 coincubation resulted in a concentration-dependent stabilization of ATB200 at neutral pH, increasing the T_m to 61.6°C at 10 μM, and 66.0°C at 100 μM, similar to that observed for the enzyme alone at acidic pH (Figure 1B). Furthermore, incubation in a neutral pH buffer (phosphate-buffered saline [PBS], pH 7.4) at 37°C resulted in time-dependent denaturation of ATB200, with the loss of 80% of its activity over a 4-hour period (Figure 1C). Again, coincubation with AT2221 resulted in a concentration-dependent protection of ATB200 activity (Figure 1C). In the presence of 17 μM AT2221, ATB200 lost only 32% of its activity (Figure 1C). Notably, 17 μM approximates the peak plasma concentration that was observed in patients with Pompe disease receiving 260 mg AT2221 (NCT02675465, ATB200-02 Amicus' ongoing clinical trial). Lastly, to better mimic the environment of infused rhGAA, ATB200 was incubated with human blood ex vivo in the presence of 17 μM AT2221 at 37°C, which again preserved ATB200 activity over the 4-hour incubation; ATB200 alone lost 63% of initial activity, whereas in the presence of AT2221 only 28% was lost (Figure 1D). These data suggest that AT2221 stabilizes ATB200 in vitro and reduces enzyme denaturation and loss of activity in blood ex vivo at concentrations that can be attained in humans.

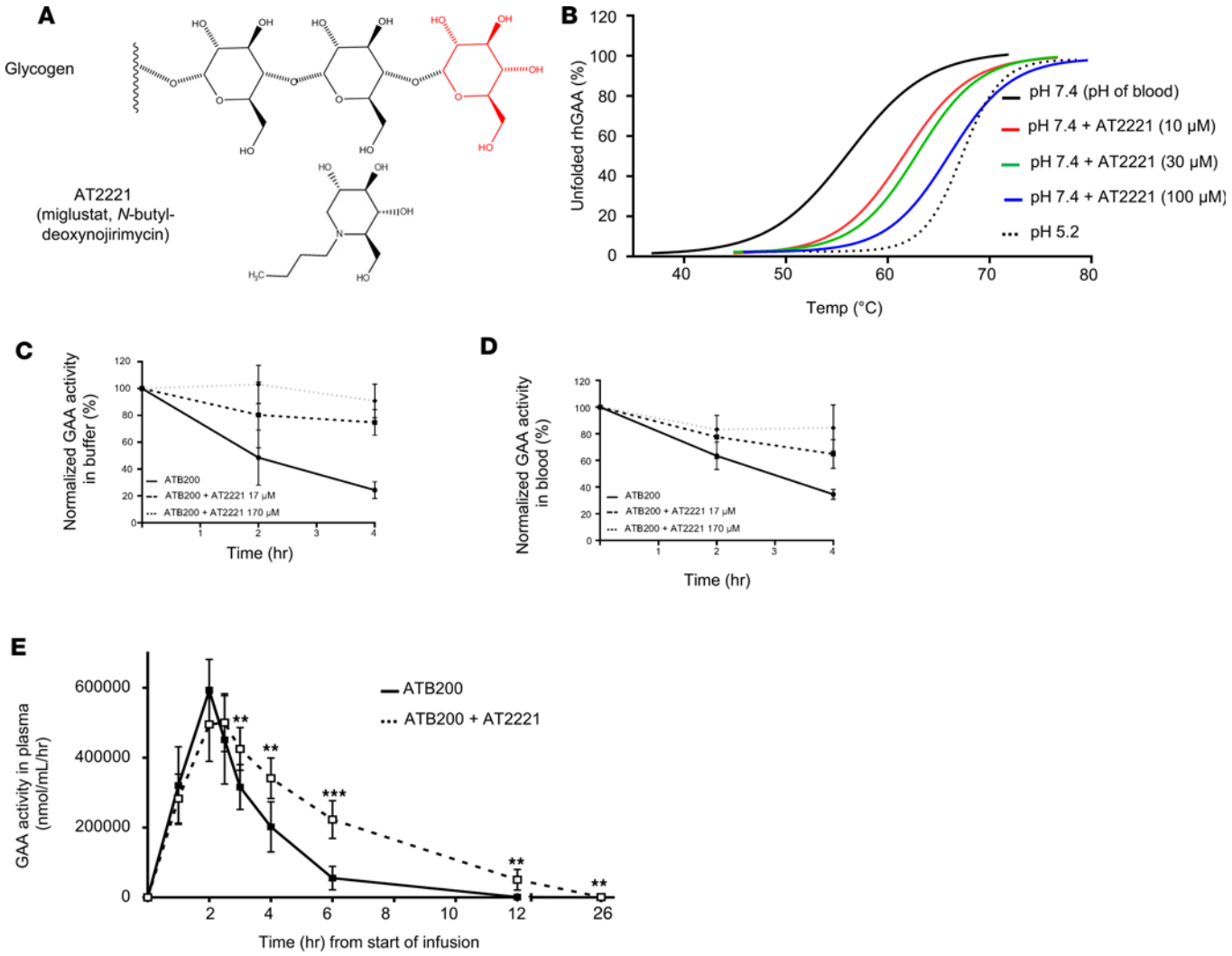

Figure 1. ATB200 is stabilized by the small-molecule pharmacological chaperone, AT2221. (**A**) AT2221 (*N*-butyl-deoxynojirimycin, miglustat) binds to and stabilizes ATB200 due to its structural similarity to the terminal glucose residue of glycogen, the natural substrate for acid α-glucosidase (GAA). (**B**) Thermostability of ATB200 alone at neutral (7.4) or acidic (5.2) pH, or in the presence of increasing concentrations of AT2221 at pH 7.4. Unfolding of ATB200 was monitored by the increase in the fluorescence of SYPRO Orange as a function of temperature. (**C** and **D**) Time course for ATB200 inactivation (i.e., loss of activity) at 37°C in PBS, pH 7.4 (**C**) or in human blood ex vivo (**D**) with and without AT2221. GAA activity at various time points was normalized to the corresponding value at time 0 (baseline activities of ATB200 alone and with 17 μM or 170 μM AT2221 were 28, 18, and 17 μmol 4MU/ml/h, respectively). (**E**) Pharmacokinetic (PK) profile of ATB200 (100 mg/kg) alone or with oral coadministration of AT2221 (175 mg/kg; 30 minutes prior to a 2-hour continuous i.v. infusion of ATB200) in cynomolgus monkeys. Blood samples were collected at the indicated time points and the PK was determined based on plasma GAA activity. $n = 4$ males and 4 females per group. Data represent mean ± SD. $^{**}P < 0.01$, $^{***}P < 0.001$ by unpaired 2-sided t test between ATB200 with and without AT2221 at each time point.

To investigate the effects of increased ATB200 stability in vivo, AT2221 was coadministered with ATB200 in nonhuman primates (cynomolgus monkeys). Oral administration of AT2221 (175 mg/kg) 30 minutes before 2-hour i.v. infusion of 100 mg/kg ATB200 (to achieve maximum physical interaction between the 2 molecules in the circulation) resulted in an approximately 2-fold increase in ATB200 exposure (Figure 1E), driven primarily by a reduction in its apparent clearance and an increase in its circulating half-life. Similar trends were seen in rodents when ATB200 and AT2221 were administered at therapeutically efficacious lower doses. Notably, 10 mg/kg AT2221 in rodents approximates the exposure of 260 mg being used in an ongoing clinical trial (NCT02675465, ATB200-02), and resulted in increased plasma half-life and exposure of ATB200 (Table 1). Collectively, these data suggest that AT2221 increases the physical stability of the exogenous enzyme and protects it from irreversible unfolding and denaturation, thereby maintaining the enzyme in a longer-lived, active form in the circulation. Hence, all subsequent studies focused on the coadministration of ATB200 with AT2221 (ATB200/AT2221) to evaluate its therapeutic effects in a *Gaa*-KO mouse model.

Table 1. Pharmacokinetics of ATB200 alone or in combination with AT2221 across several species

	ATB200 (mg/kg)	AT2221[A] (mg/kg)	AUC (×10³ nmol 4MU/ml/h × h)	$t_{1/2}$ (h)
NHP[B]	100	-	1,761	1.2
	100	175	3,140	3.1
Rat[C]	20	-	147	0.71
	20	10	183	0.82
Mouse[D]	20	-	135	0.89
	20	10	145	1.01
	20	30	147	1.06

ATB200 was administered i.v. with or without oral coadministration of AT2221 (see Methods). Plasma GAA activities were used to calculate area under the curve (AUC) and half-life values using a weighted 1-phase decay model in GraphPad Prism 7. [A]AT2221 was administered orally 30 minutes prior to ATB200 administration. [B]ATB200 was administered as a 2-hour continuous i.v. infusion; *n* = 8 monkeys (4 males and 4 females)/group. [C]ATB200 was administered as an i.v. bolus tail vein injection; *n* = 4 male rats/group. [D]ATB200 was administered as an i.v. bolus tail vein injection; *n* = 5 male *Gaa*-KO mice/group.

ATB200/AT2221 significantly improves glycogen clearance in disease-relevant muscles of Gaa-KO mice. For direct comparison of the efficacy of ATB200/AT2221 to that of alglucosidase alfa (the standard recommended dose is 20 mg/kg every 2 weeks), we have used the same dose of ATB200 in combination with 10 mg/kg AT2221; the dose of the chaperone was selected based on previous studies in *Gaa*-KO mice, with miglustat showing improved stability and uptake of rhGAA in muscle (39). The effect of ATB200/AT2221 on glycogen reduction was evaluated following 2 biweekly (over 1 month) administrations to *Gaa*-KO mice. Whereas alglucosidase alfa resulted in modest glycogen reduction in all disease-relevant muscles, the level of reduction achieved with ATB200/AT2221 was significantly greater. In quadriceps, ATB200/AT2221 reduced glycogen storage by 73%, compared with 28% by alglucosidase alfa; a similar trend was observed for triceps (42% versus 15%) and heart (85% versus 45%) (Figure 2A and Table 2). The results were further confirmed by histology using periodic acid–Schiff (PAS) staining for glycogen detection (Figure 2B). Alglucosidase alfa administration showed limited effects in skeletal muscle, whereas ATB200/AT2221 substantially reduced the number of fibers with excessive glycogen accumulation. Even in cardiac muscle, the tissue most responsive to current ERT (41), the effect of ATB200/AT2221 was greater compared with alglucosidase alfa. Importantly, the diaphragm, a tissue most affected in the Pompe population, also showed much improved glycogen clearance with ATB200/AT2221 compared with alglucosidase alfa (Figure 2B). Notably, with a longer treatment regimen (6 biweekly administrations), ATB200/AT2221 reduced glycogen accumulation in both cardiomyocytes and cardiac vascular smooth muscle cells. In contrast, the efficacy of alglucosidase alfa seemed to be restricted only to cardiomyocytes (Figure 2C). These data demonstrated superiority of ATB200/AT2221 in reducing glycogen compared with alglucosidase alfa, which was apparent after only 2 administrations of the drugs.

The greater effect of ATB200/AT2221 is believed to be due to higher levels of M6P, which leads to enhanced lysosomal targeting in muscle. This is demonstrated by the much higher levels of the processed, mature lysosomal form of rhGAA (76 kDa) compared with the levels observed following alglucosidase alfa administration (Figure 2D). Furthermore, this mature form of GAA is known to have a higher affinity and activity towards glycogen (29, 42, 43), which leads to a more effective substrate reduction.

ATB200/AT2221 substantially reduces lysosomal expansion and autophagic buildup in disease-relevant muscles of Gaa-KO mice. The enlargement of glycogen-loaded lysosomes is a hallmark of Pompe disease (1). Immunohistochemical (IHC) analysis of muscle samples using an anti–lysosome-associated membrane protein 1 (anti-Lamp1) antibody demonstrated a dramatic increase in the number of Lamp1-positive structures in all muscles examined (quadriceps, heart, and diaphragm) in *Gaa*-KO mice compared with age-matched wild-type (WT) animals (Figure 3A). Although 2 biweekly administrations of alglucosidase alfa had a limited effect on the Lamp1 signal in these tissues, ATB200/AT2221 led to a clear reduction in the signal, with near-complete clearance in the majority of muscle fibers (Figure 3A and Supplemental Figure 1; supplemental material available online with this article; https://doi.org/10.1172/jci.insight.125358DS1). Notably, quadriceps, a predominantly type II muscle known to be resistant to ERT with alglucosidase alfa (44), responded well to ATB200/AT2221. Although limited overall, the effect of alglucosidase alfa on Lamp1 signal reduction was indeed more pronounced in type I muscle fibers, as shown by IHC using a slow myosin heavy chain–specific antibody (clone NOQ7.5.4D; labels type I muscle fibers) in combination with Lamp1 staining on adjacent sections (Supplemental Figure 2). In con-

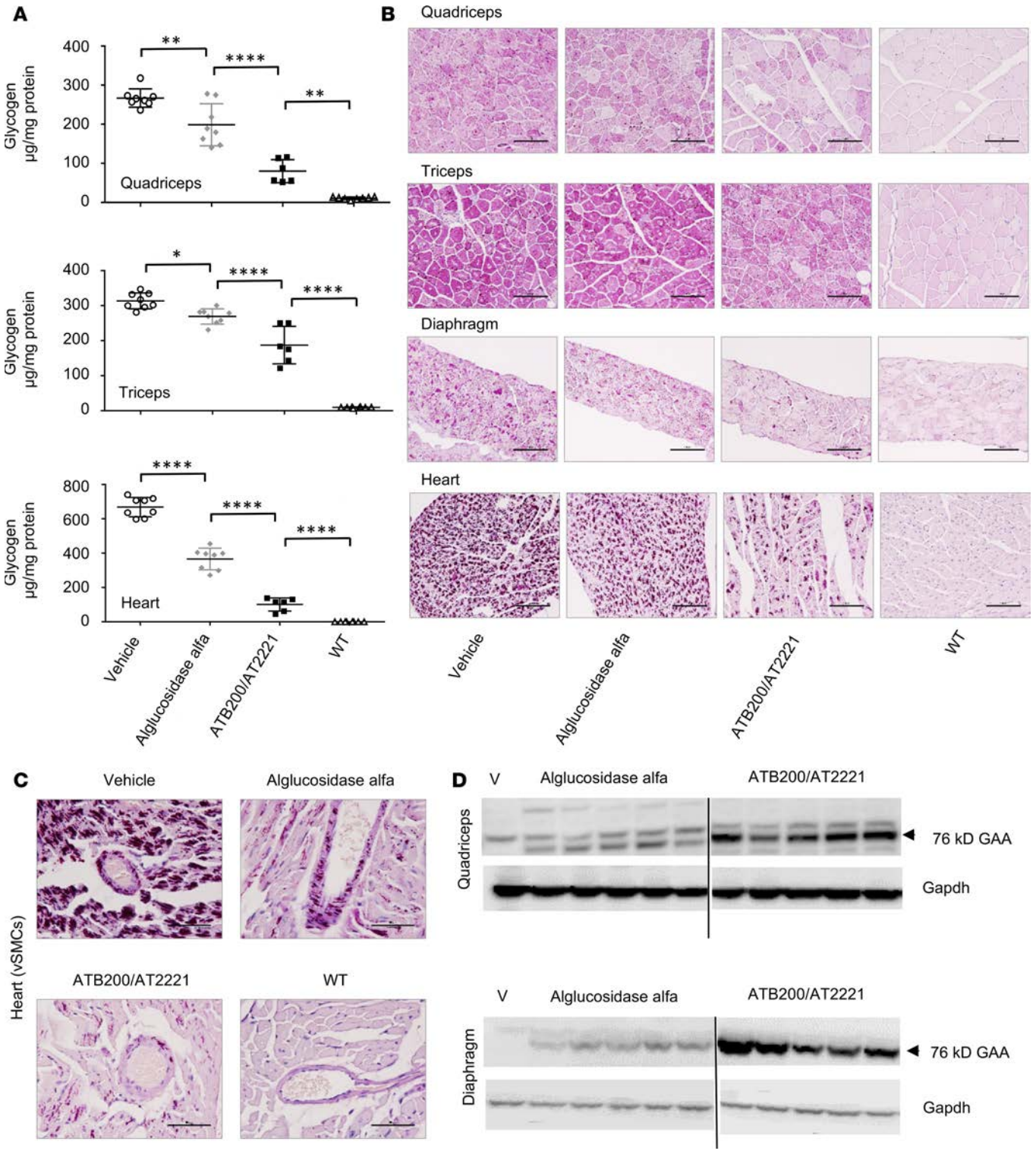

Figure 2. ATB200/AT2221 exhibits better glycogen clearance and greater lysosomal targeting in vivo compared with alglucosidase alfa. Male *Gaa*-KO mice (14–16 weeks old) received 2 (**A** and **B**) or 6 (**C**) biweekly i.v. administrations of vehicle, 20 mg/kg alglucosidase alfa, or 20 mg/kg ATB200/AT2221 (10 mg/kg AT2221 was administered orally 30 minutes prior to ATB200 i.v. injection). Tissues were collected 14 days after the last administration. (**A**) Glycogen levels in different skeletal muscles and in the heart. Individual values and mean ± SD are shown. n = 6–8 animals per group. $^{*}P < 0.05$, $^{**}P < 0.01$, $^{***}P < 0.001$, $^{****}P < 0.0001$ by Tukey's multiple comparison under 1-way ANOVA. (**B**) PAS staining for glycogen in paraffin sections of muscle tissues. n = 6–8 animals per group. Original magnification, ×200. Scale bars: 100 µm. (**C**) PAS staining for glycogen in cardiac vascular smooth muscle cells (vSMCs). n = 7 animals per group. Original magnification, ×400. Scale bars: 50 µm. (**D**) Western blot of muscle lysates from quadriceps and diaphragm derived from 22-week-old alglucosidase alfa– and ATB200/AT2221–treated mice after a single administration. Tissues were collected 3 days after administration.

Table 2. ATB200/AT2221 reduces muscle glycogen levels in *Gaa*-KO mice more efficiently than alglucosidase alfa

	Glycogen Reduction (%)	
Tissue	**Alglucosidase alfa**	**ATB200/AT2221**
Quadriceps	27.5 ± 19.5	72.9 ± 11.5
Gastrocnemius	21.2 ± 11.5	78.6 ± 2.6
Triceps	14.6 ± 7.1	41.5 ± 17.6
Heart	45.2 ± 9.4	84.9 ± 5.7

Male *Gaa*-KO mice (~16 weeks old) received 2 biweekly administrations of 20 mg/kg alglucosidase alfa or 20 mg/kg ATB200/AT2221. Glycogen levels were measured in tissues collected 14 days after the last administration (See also Figure 2). To calculate percentage reduction, the amount of glycogen in the WT was subtracted from average glycogen levels in untreated and treated *Gaa*-KO mice. Data represent the mean ± SD; n = 6–8 mice per group.

trast, ATB200/AT2221 reduced Lamp1 signals to near-normal levels in both type I and type II fibers, indicating its ability to reduce/reverse lysosomal pathology in muscles regardless of their fiber type composition.

Muscle defects in patients with Pompe disease and *Gaa*-KO mice extend beyond glycogen accumulation and lysosomal proliferation (22, 45). Autophagic buildup, a telltale signal of muscle damage in Pompe disease, was shown to negatively affect the trafficking and lysosomal delivery of alglucosidase alfa (45–47). Methylene blue staining and transmission electron microscopy (TEM), indeed, revealed abundant autophagic vacuoles with accumulated cellular debris in the quadriceps of *Gaa*-KO mice (Figure 3B). IHC examination of autophagy on paraffin sections using an antibody against microtubule-associated protein 1A/1B light chain 3 (LC3; autophagosomal marker) revealed signals in *Gaa*-KO muscle but not in WT controls. The LC3-positive aggregates in *Gaa*-KO muscle fibers overlapped with SQSTM1/p62-positive structures (Figure 3C); SQSTM1/p62 is an autophagic substrate that links ubiquitinated proteins to autophagosomes (48, 49). Following 2 biweekly administrations, ATB200/AT2221, but not alglucosidase alfa, appeared to reduce autophagic accumulation as shown by TEM and by IHC with LC3 and SQSTM1/p62 antibodies (Figure 3, B and C). These data were supported by Western blotting of whole-muscle (quadriceps) lysates with the LC3 antibody (Supplemental Figure 3).

Considering this unexpected effect of ATB200/AT2221 on autophagy, another set of experiments was designed to have a closer look at the consequences of ATB200/AT2221 administration. Four biweekly administrations of ATB200/AT2221 or alglucosidase alfa were given to approximately 16-week-old *Gaa*-KO mice. Similar to what was observed after 2 administrations, there was a striking difference in the degree of glycogen clearance between the 2 groups; biochemical analysis of yet another muscle group (gastrocnemius) showed a much more efficient reduction of glycogen in ATB200/AT2221–treated mice compared with alglucosidase alfa–treated mice (Figure 4A). Again, consistent with the results of the study with 2 biweekly administrations, the mature lysosomal form of GAA was far more abundant in ATB200/AT2221–treated mice, leading to a greater reduction in the levels of Lamp1, LC3-II, and the autophagy-specific substrate SQSTM1/p62 compared with those after alglucosidase alfa administration (Figure 4, B–E). LC3 exists as a soluble form, LC3-I, and an autophagosome membrane–bound LC3-II form, and the amount of the latter correlates well with the extent of autophagosomal formation (50).

Immunostaining of single muscle fibers for Lamp1 and LC3 showed extensive Lamp1- and LC3-positive areas of autophagic accumulation (often located in the core of myofibers) in both vehicle- and alglucosidase alfa–treated *Gaa*-KO mice; more than 95% of the fibers still contained autophagic buildup despite treatment (n = 141 fibers from 4 mice) (Figure 5). In contrast, the number of fibers with typical buildup fell dramatically to less than 30% in ATB200/AT2221–treated mice (n = 127 fibers from 4 mice) (Figure 5). The remaining fibers contained buildup of different smaller sizes; this spectrum most likely represents stages of autophagic resolution in the diseased muscle (Figure 5 and Supplemental Figure 4, A and B). Of note, unlike alglucosidase alfa–treated mice, the majority of fibers from ATB200/AT2221–treated mice showed little (if any) lysosomal enlargement outside the buildup areas, and many (approximately 50%) appeared indistinguishable from the WT (Figure 5).

We have also used second harmonic generation (SHG) microscopy (51), a technique that allows visualization of myosin bands in unstained muscle tissue (52). When combined with 2-photon excited fluorescence (2PEF) of mitochondrial and lysosomal components, the technique provides detailed structural information on

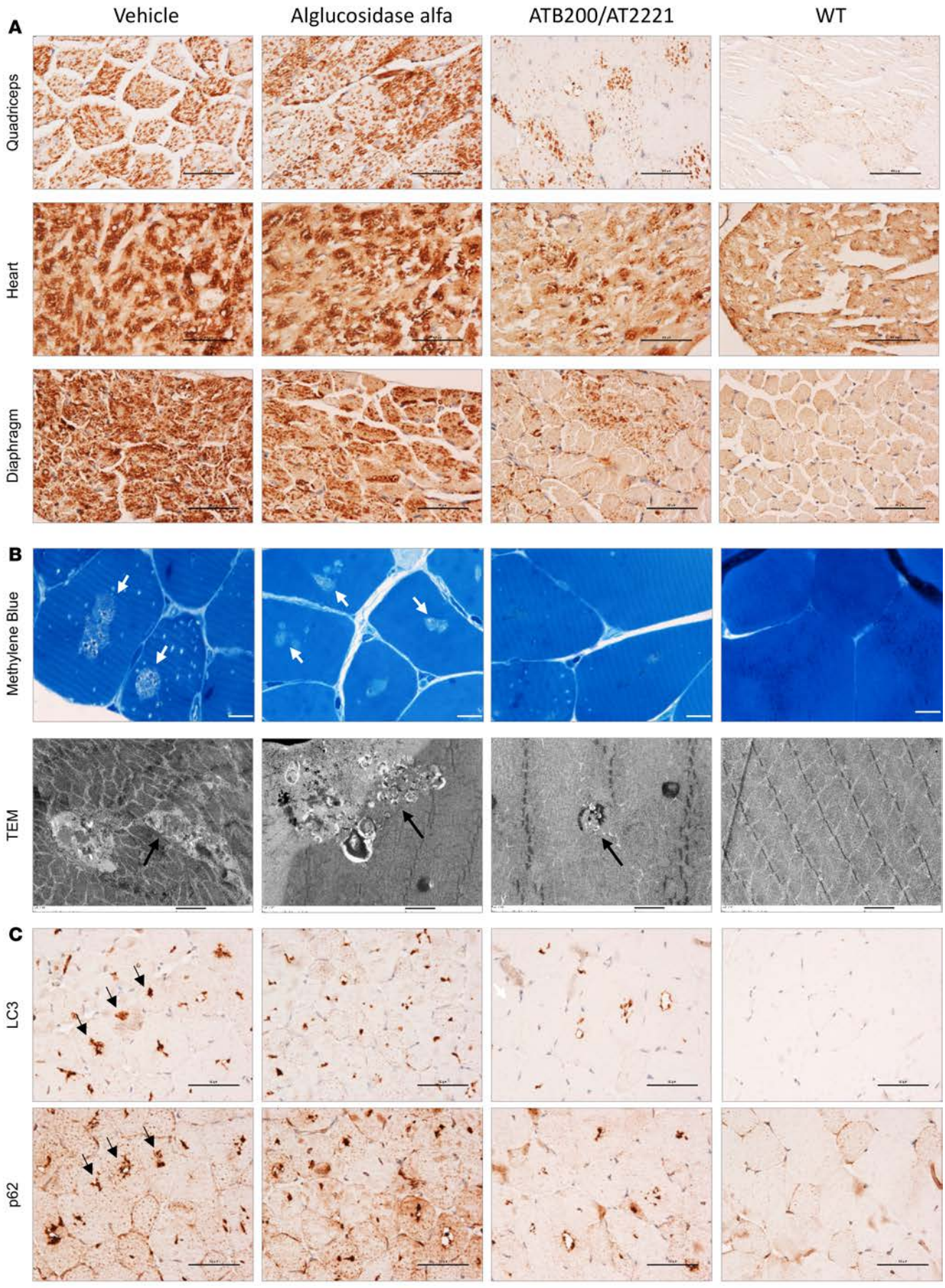
Vehicle
Alglucosidase alfa
ATB200/AT2221
WT
A
Quadriceps
Heart
Diaphragm
B
Methylene Blue
TEM
C
LC3
p62

Figure 3. ATB200/AT2221 corrects lysosomal and autophagic pathologies in *Gaa*-KO mice. Sixteen-week-old male *Gaa*-KO mice received 2 biweekly administrations of vehicle, alglucosidase alfa, or ATB200/AT2221 at doses and routes as described in the legend for Figure 2. Tissues were collected 14 days after the second administration. (**A**) Lamp1-stained (lysosomal marker) sections of skeletal muscle (quadriceps), heart, and diaphragm tissues from vehicle-, alglucosidase alfa–, or ATB200/AT2221–treated *Gaa*-KO, and untreated WT mice. n = 4–5 animals per group (n = 2 for the WT) (see Supplemental Figure 1 for statistical analysis). Original magnification, ×400. Scale bars: 50 μm. (**B**) Methylene blue–stained sections (top) and transmission electron microscopy (TEM; bottom) of quadriceps from different animal groups (as in **A**). Arrows point to the area occupied by autophagic buildup. Original magnification, ×1,000 (top) and ×5,000 (bottom). Scale bars: 10 μm (top) and 2 μm (bottom). (**C**) LC3-stained (autophagosomal marker; top) and SQSTM/p62-stained (bottom) sections of quadriceps from different animal groups (as in **A**). n = 4–5 animals per group (n = 2 for the WT). Original magnification, ×400. Scale bars: 50 μm.

unstained muscle bundles. As we reported previously, untreated *Gaa*-KO muscles show small and large holes interrupting muscle architecture; the small holes correspond to nuclei and enlarged lysosomes, whereas the large ones represent the inclusions of autophagic debris containing fluorescent materials (53). The areas of autophagic accumulation remained prominent in muscle from alglucosidase alfa–treated mice but were much reduced in size and number following ATB200/AT2221 treatment (Figure 6 and Supplemental Figure 5). Consistent with the data obtained with single muscle fibers, a majority of ATB200/AT2221–treated fibers appeared normal.

The reversal of lysosomal and autophagic pathologies in ATB200/AT2221–treated muscle was associated with the appearance of normal morphology of postsynaptic acetylcholine receptor (AChR) at the neuromuscular junction and restoration of microtubular networks as shown by labeling with α-bungarotoxin and anti–α-tubulin, respectively (Supplemental Figure 6). Taken together, the data indicate that treatment with ATB200/AT2221 is more efficient in reversing skeletal muscle pathology in murine Pompe disease.

In addition, we looked at the phosphorylation status of glycogen synthase kinase 3β (GSK-3β), a protein long known to play an important role in regulating glycogen synthesis. In agreement with our previous data (54), a decrease in phosphorylation (activation) of GSK-3β (p-GSK S9) leading to an increase in phosphorylation (inactivation) of glycogen synthase (p-GS S641) was seen in muscle from untreated *Gaa*-KO mice. The phosphorylation levels of p-GSK S9 and p-GS S641 did not change after alglucosidase alfa treatment (Figure 7, A and B). In contrast, ATB200/AT2221–treated muscle showed a significant increase in the levels of p-GSK S9 (although not fully reaching the WT levels) and a decrease in p-GS S641 to the WT levels, suggesting a return of glycogen synthesis/stores to normal, which may contribute to the improved functional outcome.

ATB200/AT2221 improves muscle function in Gaa-KO mice. Muscle function was evaluated in *Gaa*-KO mice using the grip-strength and wire-hang tests. *Gaa*-KO mice showed poor performance and progressive deterioration with age when compared with WT mice in both tests (Figure 8, A and B). The grip strengths of ATB200/AT2221–treated, but not alglucosidase alfa–treated mice, gradually improved starting from 2 months (i.e., 4 biweekly administrations) and approached the level of age-matched WT mice over the 5-month treatment period (Figure 8A). In the wire-hang test, ATB200/AT2221 treatment prevented decline over the 5-month period (Figure 8B), with the mice consistently showing the tendency to perform better compared with alglucosidase alfa–treated mice.

Upon completion of the functional assessments, the mice were given 2 additional administrations of vehicle, alglucosidase alfa, or ATB200/AT2221 (12 administrations total), followed by assessment of muscle fiber size using minimum Feret's diameter (Min FD; Figure 8, C and D). Muscle atrophy is a prominent feature in Pompe disease (45, 55, 56) as well as in other myopathies and muscular dystrophies (57), and in aging (58). The fiber size from vehicle-treated *Gaa*-KO mouse quadriceps was much smaller than that of the age-matched WT mice (31 ± 1.5 versus 45 ± 4 μm), with an increased population of smaller fibers. Alglucosidase alfa administration resulted in only very small increases in the Min FD compared with the vehicle control (32 ± 1.6 versus 31 ± 1.5 μm), whereas ATB200/AT2221 administration led to a shift towards the larger fibers, with a significant increase in Min FD value (37 ± 2 μm) compared with alglucosidase alfa or vehicle ($P < 0.05$). Importantly, the changes in muscle fiber size paralleled those in muscle strength.

We also explored other factors that may contribute to muscle weakness in Pompe disease. The likely candidates are those involved in muscular dystrophies, as Pompe disease can be misdiagnosed as one (59, 60). We have found an abnormal accumulation of dysferlin, a transmembrane protein, in the sarcoplasm of myofibers from different muscle groups in *Gaa*-KO mice (Figure 8E). Alterations in sarcolemmal dysferlin protein levels, caused by mutations or mislocalization, have been linked to several forms of limb-girdle muscular dystrophy (61–64). Although long-term administration of alglucosidase alfa (12 administrations total in 6 months) resulted in no or limited change in the intracellular accumulation of dysferlin, there was a notable reduction in both quadriceps and triceps of *Gaa*-KO mice following

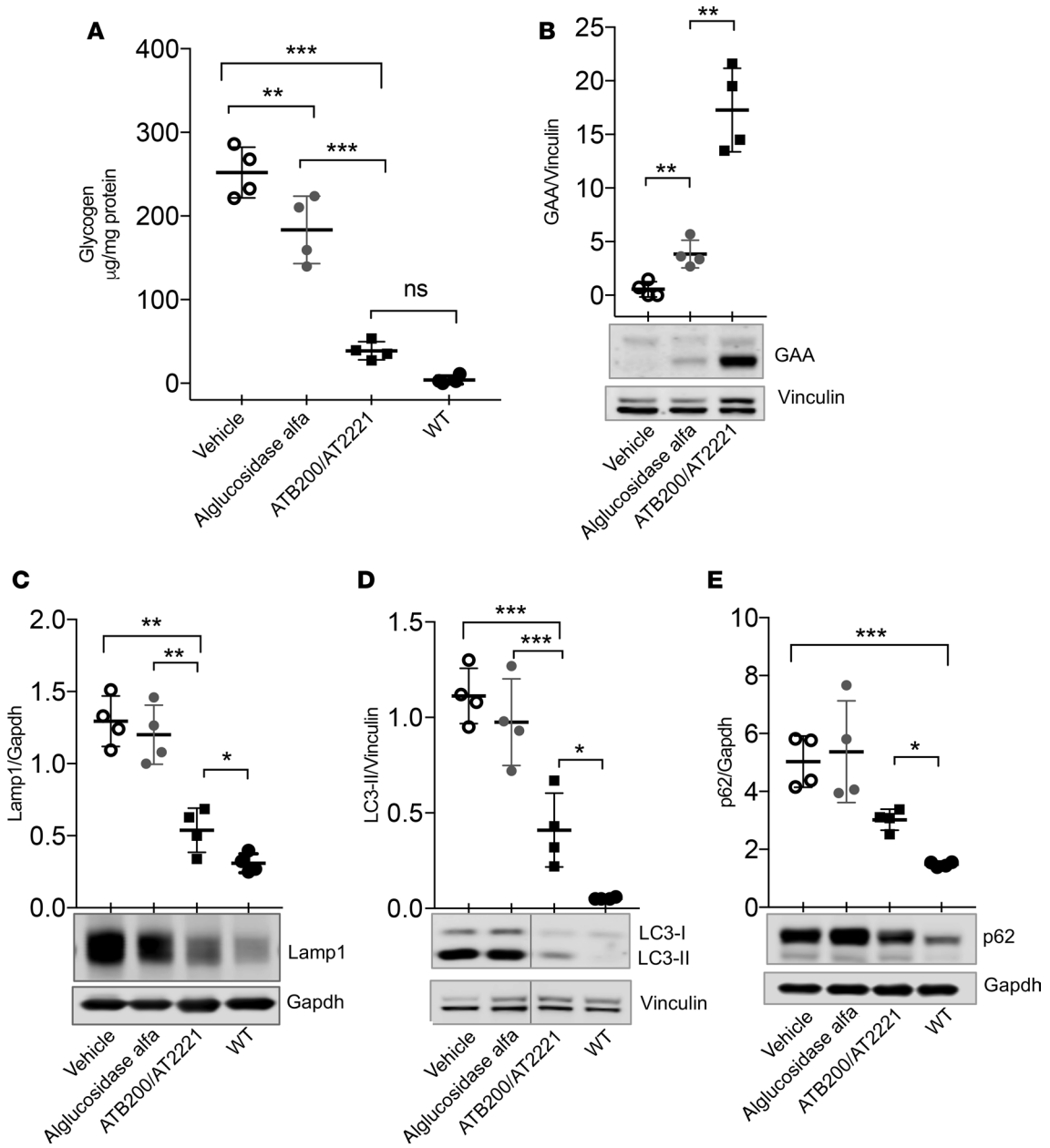

Figure 4. ATB200/AT2221 is more efficient than alglucosidase alfa in reducing glycogen storage and the levels of lysosomal and autophagosomal markers in muscle from *Gaa*-KO mice. Sixteen-week-old male *Gaa*-KO mice received 4 biweekly administrations of vehicle, alglucosidase alfa, or ATB200/AT2221 at doses and routes as described in the legend for Figure 2. Muscle samples were collected 14 days after the last administration. The white part of gastrocnemius muscle was isolated for the experiments. (**A**) Glycogen content in muscles from vehicle-, alglucosidase alfa–, or ATB200/AT2221–treated *Gaa*-KO, and untreated WT mice. (**B**–**E**) Representative images of Western blot analyses of whole-muscle lysates with the indicated antibodies. Gapdh or vinculin was used as loading control. $n = 4$ mice from each group. Representative images are shown. Each lane represents a sample from a single mouse. The lanes in **D** were run in the same gel but were noncontiguous. Individual values and mean ± SD are shown. ns, not significant. $^*P < 0.05$, $^{**}P < 0.01$, $^{***}P < 0.001$ by Student's *t* test.

ATB200/AT2221 treatment (Figure 8E).

Overall, we have shown that in every measured outcome — glycogen clearance, lysosomal enlargement and autophagic buildup, muscle fiber size, and muscle strength — ATB200/AT2221 is superior to alglucosidase alfa in the murine model of Pompe disease.

Discussion

The limitations of current ERT in treating skeletal muscle in Pompe disease are now well recognized,

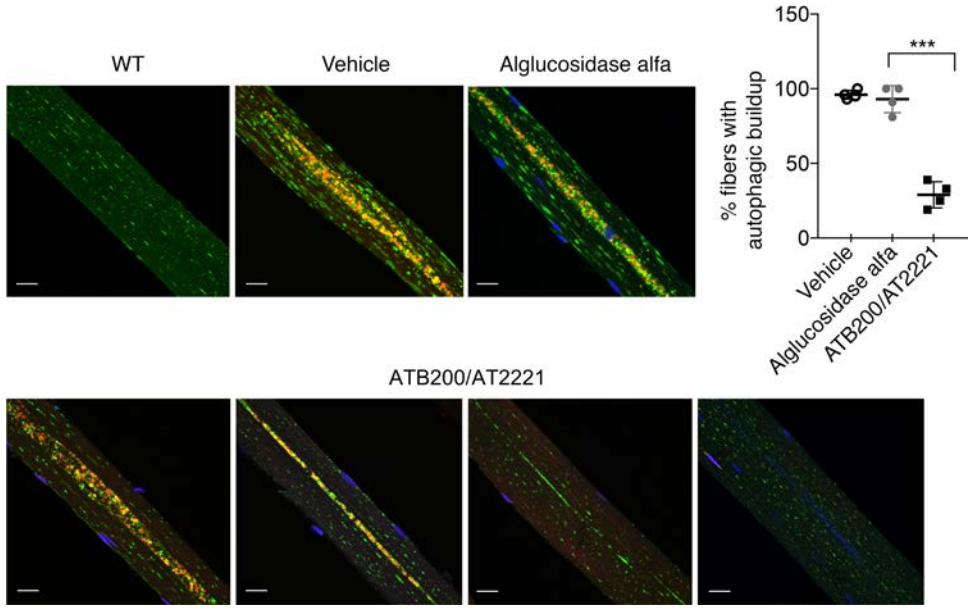

Figure 5. ATB200/AT2221 alleviates autophagic buildup in muscle from *Gaa*-KO mice. Sixteen-week-old male *Gaa*-KO mice received 4 biweekly administrations of vehicle, alglucosidase alfa, or ATB200/AT2221 at doses and routes as described in the legend for Figure 2. The white part of gastrocnemius was collected 14 days after the last administration. Immunostaining of single fibers with markers for lysosomes (Lamp1; green), autophagosomes (LC3; red), and nuclei (Hoechst dye; blue); the multicolored areas in the core of muscle fibers represent autophagic buildup. Lysosomes appear as numerous dot-like Lamp1-positive structures in WT fibers. Enlarged lysosomes and autophagic buildup are seen in the majority of fibers from vehicle- and alglucosidase alfa–treated *Gaa*-KO mice (top panels). The dot plot indicates the percentage of fibers with autophagic buildup in each group. A significant reduction in the number of fibers with autophagic buildup is seen in ATB200/AT2221–treated mice (all fibers with autophagic accumulation were counted, irrespective of the buildup size). The 4 bottom panels show variability in the size of autophagic buildup in ATB200/AT2221–treated mice. n = 141 fibers from 4 alglucosidase alfa–treated *Gaa*-KO mice; n = 127 fibers from 4 ATB200/AT2221–treated *Gaa*-KO mice. Individual values and mean ± SD are shown. ***$P < 0.001$ by Tukey's multiple comparison under 1-way ANOVA. Scale bars: 20 μm.

and new therapeutic approaches are being investigated. The deficiency of current ERT is mainly attributed to the poor lysosomal targeting/uptake of alglucosidase alfa due to its low M6P content. Unlike the previous approaches designed to improve the uptake by either chemical glycoengineering (32, 33) or by fusion to the GILT tag (34), our proprietary cell line yields an rhGAA, ATB200, with substantially higher M6P content and affinity for the CI-MPR compared with alglucosidase alfa, leading to greater lysosomal targeting in muscle cells. ATB200 is being developed as a next-generation Pompe ERT in combination with the small-molecule PC, AT2221. AT2221 binds to and stabilizes ATB200, thus preventing its denaturation and improving its PK properties. A preliminary proof-of-concept study showed improved PK of alglucosidase alfa coadministered with oral miglustat in Pompe patients, but the combination protocol did not appreciably improve the clinical outcome (37), most likely because the enzyme activity in muscles was not sufficiently increased.

At a dose of 20 mg/kg, ATB200 coadministered with 10 mg/kg AT2221 orally (ATB200/AT2221) was taken up and delivered to lysosomes in skeletal muscles of *Gaa*-KO mice more efficiently than was alglucosidase alfa (20 mg/kg), as evidenced by significantly higher amounts of the mature lysosomal form of GAA. The exact amount of mature lysosomal form needed to reverse established disease is not clear, but the assumption is that levels close to 50% of normal would be sufficient since Pompe disease is an autosomal recessive disorder. However, our data using transgenic *Gaa*-KO mice expressing human *Gaa* indicate that much higher levels are required for the reversal of preexisting pathology (23). In fact, the levels achieved with ATB200/AT2221 were far greater than those seen with alglucosidase alfa. These increased levels of mature lysosomal GAA translated into significantly greater glycogen reduction in skeletal muscles. Furthermore, ATB200/AT2221 was able to clear glycogen accumulation in smooth muscle cells of the cardiac blood vessels. Although little attention has been focused on cardiac smooth muscle cells in Pompe dis-

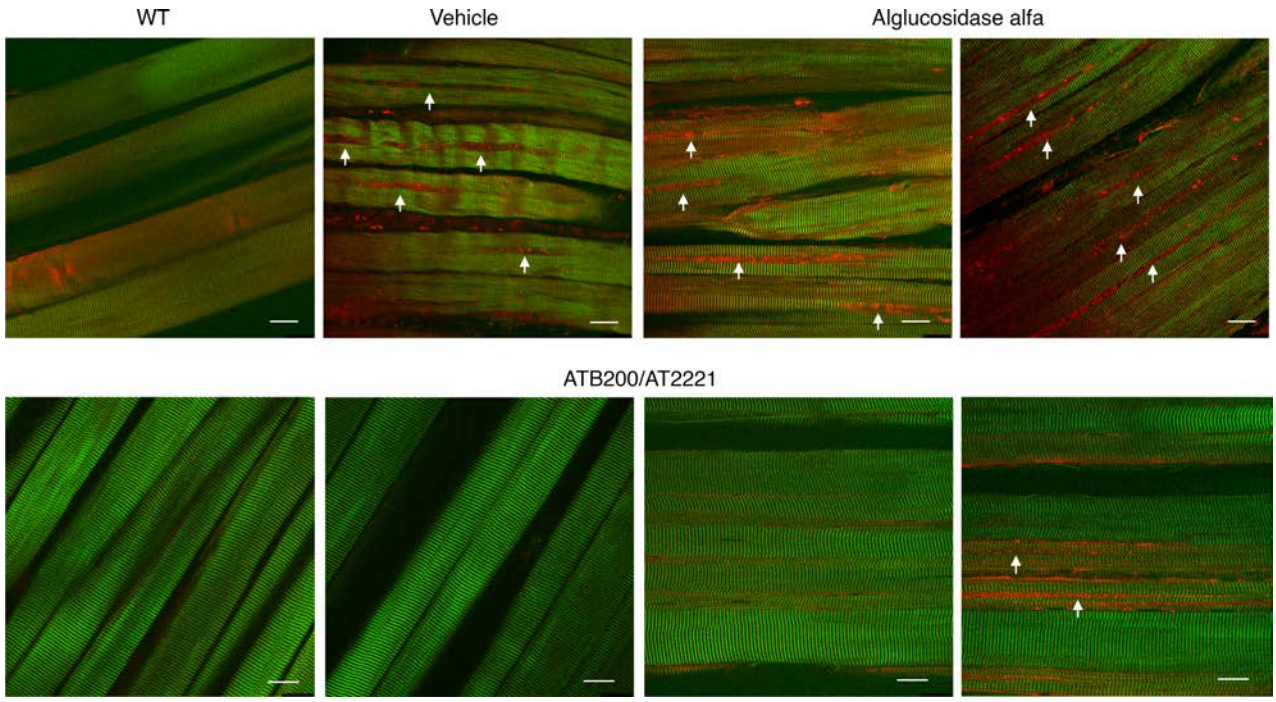

Figure 6. Second harmonic generation (SHG) and 2PEF imaging show improvement in fibers from ATB200/AT2221–treated *Gaa*-KO mice. Sixteen-week-old male *Gaa*-KO mice received 4 biweekly administrations of vehicle, alglucosidase alfa, or ATB200/AT2221 at doses and routes as described in the legend for Figure 2. The white part of gastrocnemius was collected 14 days after the last administration. To assess the quality of muscle bundles, each sample was mounted in 90% glycerol in a chamber made with spacers between a slide and a coverslip. The fibers were then excited at 870 nm to collect the SHG imaging signal (green) and the 2-photon excited fluorescence signal (2PEF, red) as previously described (53). SHG reflects the position and organization of myosin heavy chain, while 2PEF reflects mitochondria and autofluorescent particles such as lipofuscin. WT fibers show a well-organized SHG signal and little 2PEF except where mitochondria are concentrated along the blood vessels at the surface of one of the fibers (arrowhead). In contrast, fibers from vehicle-treated and alglucosidase alfa–treated *Gaa*-KO mice show long interruptions of the SHG image that are rich in 2PEF-positive particles (arrows); these areas correspond to the space occupied by autophagic debris. In ATB200/AT2221–treated mice, some areas still show such a defect (arrows), but many areas appear indistinguishable from WT. Scale bars: 25 μm.

ease, a number of recent reports point to cardiac and intracranial vascular abnormalities in LOPD patients leading to stroke and death in some cases (65–69). The benefit of ATB200/AT2221 in cardiac smooth muscle cells may become more apparent as the life expectancy of patients with Pompe disease continues to rise and the previously unknown or neglected pathologies are revealed. Furthermore, ATB200/AT2221 may provide relief of the symptoms associated with glycogen accumulation in other organs containing smooth muscle, such as the bladder, intestine, and esophagus (70, 71).

The accumulation of glycogen in lysosomes leads to the expansion/hyperproliferation of lysosomal-endocytic compartments (45, 72). ATB200/AT2221 treatment led to a dramatic reduction in the number of Lamp1-positive structures in the majority of muscle fibers, and to an overall decrease in the amount of Lamp1 protein, again, outperforming alglucosidase alfa. Notably, ATB200/AT2221 reduced lysosomal burden in both slow-twitch type I and fast-twitch type II fibers — a clear improvement over the current standard of care, which shows some effect in type I but little-to-no effect in type II myofibers, consistent with our previous observations (44). The relatively low abundance of CI-MPR in type II muscle, no doubt, contributes to the suboptimal efficacy of alglucosidase alfa (73, 74), but it is equally clear that the receptor number is not the only limiting factor; when the affinity for the receptor is enhanced, as is the case with ATB200/AT2221, the drug can be efficiently transported to the lysosome and clear glycogen in disease-relevant muscle tissues.

We have previously shown that pathology in the diseased muscle extends beyond lysosomes and involves defective autophagy (75), a major intracellular lysosome-dependent recycling pathway (76). Massive autophagic buildup runs along the length of muscle fibers, damaging the muscle architecture and contractile apparatus (77) and interfering with the trafficking of alglucosidase alfa (21, 45). According to the mitochondrial/lysosomal axis theory of aging, this buildup can be referred to as "biological garbage" (78). Once formed, autophagic pathology persists despite alglucosidase alfa treatment (16, 44). To overcome this shortcoming, several experimental autophagy-targeted therapeutic approaches have been tested. These

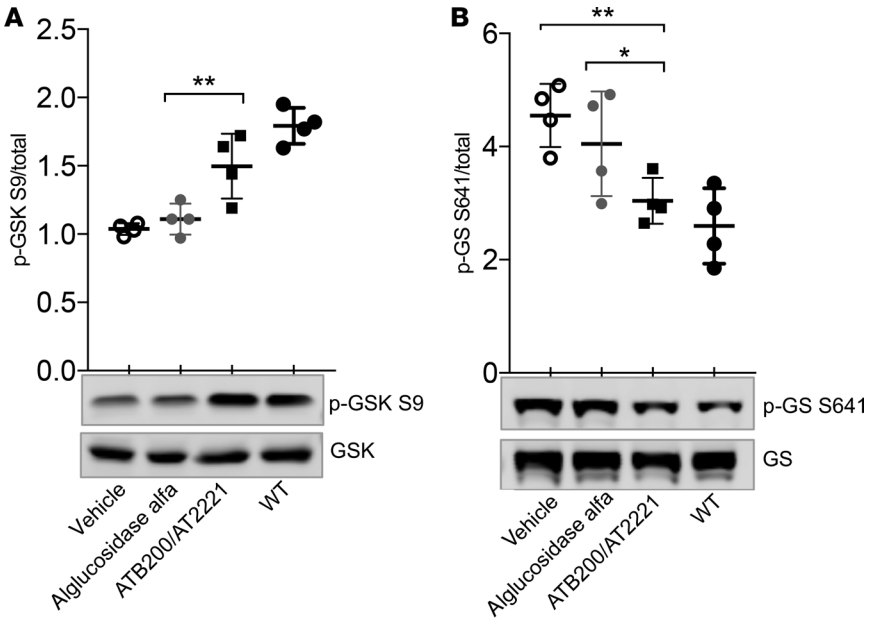

Figure 7. ATB200/AT2221 affects metabolic changes in muscle from *Gaa*-KO mice. Sixteen-week-old male *Gaa*-KO mice received 4 biweekly administrations of vehicle, alglucosidase alfa, or ATB200/AT2221 at doses and routes as described in the legend for Figure 2. Muscle samples were obtained 14 days after the last administration. Representative images of Western blot analysis of whole muscle (white part of gastrocnemius) lysates from vehicle-, alglucosidase alfa–, or ATB200/AT2221–treated *Gaa*-KO, and untreated WT mice with the indicated antibodies. A markedly decreased phosphorylation (activation) of GSK-3β (**A**; p-GSK S9) and increased phosphorylation (inactivation) of glycogen synthase (**B**; p-GS S641) in *Gaa*-KO muscle (consistent with our previously reported data; see ref. 54) are reversed in ATB200/AT2221–treated mice. $n = 3$ mice from WT; $n = 4$ from each of the other 3 groups. Representative images are shown. Each lane represents a sample from a single mouse. Individual values and mean ± SD are shown. $^*P < 0.05$, $^{**}P < 0.01$ by Student's t test.

include genetic suppression of autophagy by inactivation of a key autophagic gene, *ATG7*; overexpression of transcription factors TFEB and TFE3 to stimulate autophagosomal-lysosomal fusion and lysosomal exocytosis; and inhibition of autophagy by upregulation of mammalian target of rapamycin complex 1 (mTORC1) (46, 79, 80). However, these strategies are currently not a substitute for ERT.

Here we show that ATB200/AT2221 leads to an impressive increase in the number of muscle fibers free from autophagic buildup, thus providing the first piece of evidence. To our knowledge to suggest that the buildup can be resolved by ERT. Several possibilities may explain this somewhat unexpected and quite dramatic effect of ATB200/AT2221 on the reversal of autophagic pathology. We hypothesize that speedy and efficient lysosomal glycogen clearance creates a pool of normally functioning lysosomes with high degradative capacity able to clear the accumulated debris. An additional possibility is that the drug (by virtue of its much better muscle targeting compared with alglucosidase alfa) may degrade glycogen within autophagosomes themselves, thus making them more likely to fuse with lysosomes. We and others have previously demonstrated that the autophagic pathway is at least partially responsible for the delivery of glycogen to the lysosomal compartment, and the accumulation of glycogen in autophagosomes is well documented (54, 81, 82). However, the exact mechanism of ATB200/AT2221–mediated reversal of the autophagic defect in the muscles affected by Pompe disease remains to be further investigated.

A greater overall decrease in glycogen storage following ATB200/AT2221 treatment (as compared with alglucosidase alfa) combined with the elimination of noncontractile autophagic debris in many fibers was associated with increased muscle strength. We have previously reported an increase in myofiber force in untreated *Gaa*-KO mice in which the buildup was removed by genetic suppression of autophagy (83). In addition, ATB200/AT2221 corrected several other abnormalities in Pompe muscles, such as muscle fiber size, phosphorylation status of glycogen synthase, and localization of dysferlin. The loss of muscle mass leading to profound muscle weakness is one of the major clinical manifestations of the disease (1). Indeed, significant fiber size reduction was observed in quadriceps from *Gaa*-KO mice compared with age-matched WT animals, consistent with our previous data in other muscle groups (56, 79, 80). The increase in fiber size following ATB200/AT2221 treatment correlated well with the improvement in muscle strength.

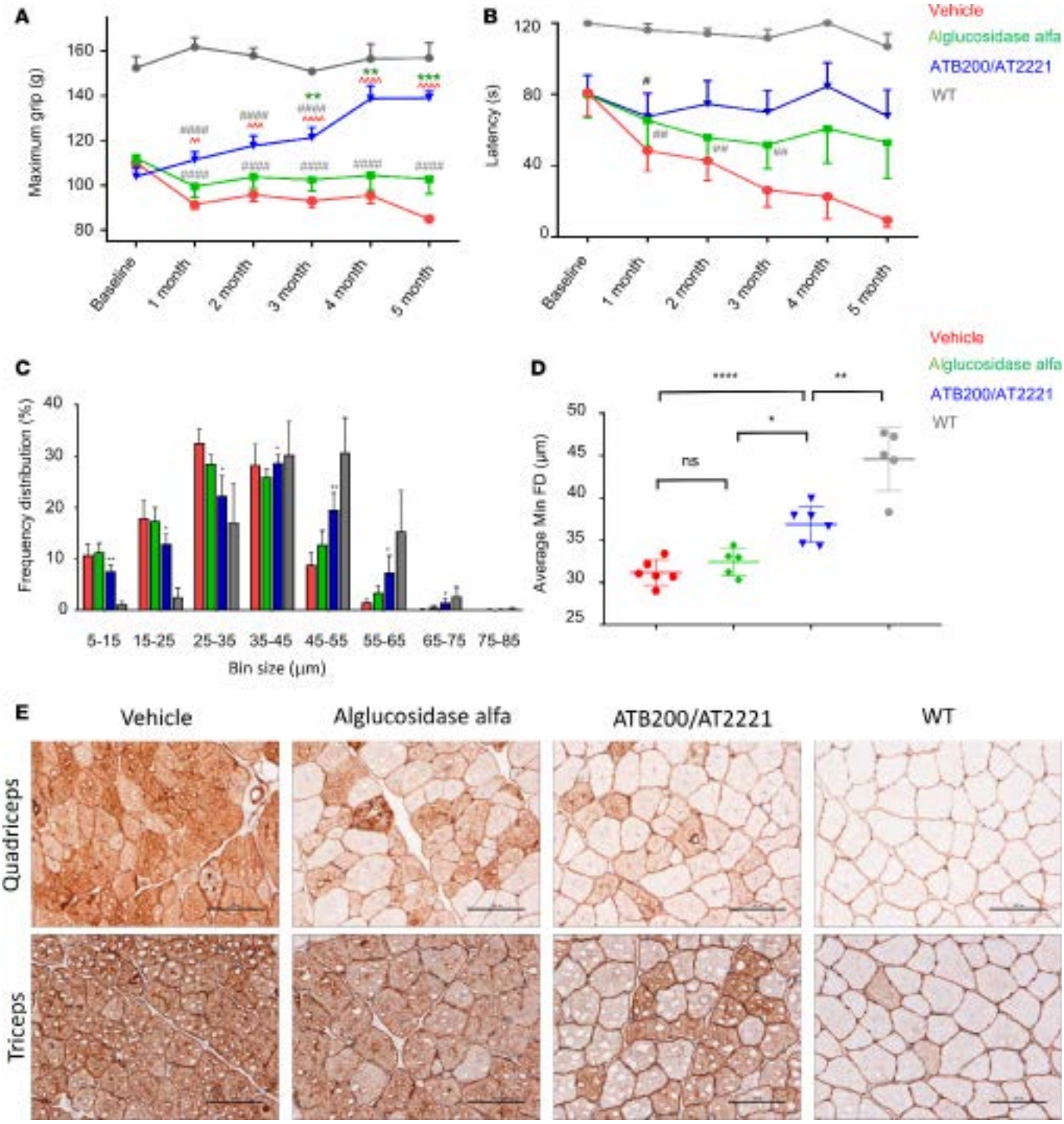

Figure 8. Long-term administration of ATB200/AT2221 improves muscle function in *Gaa*-KO mice. Fourteen-week-old male *Gaa*-KO mice received 10 biweekly administrations of vehicle, alglucosidase alfa, or ATB200/AT2221 at doses and routes as described in the legend for Figure 2. A group of age-matched untreated WT mice was included for comparison. Muscle strength was assessed using grip-strength (**A**) and wire-hang (**B**) tests every month. Data represent the mean ± SEM. n = 12–15 mice/group for baseline and the first 3 months; n = 6–8 mice/group for months 4 and 5 (7 animals from each group were euthanized after 3 months for interim analysis). Multiple comparison was performed for grip-strength and wire-hang data using 1-way ANOVA and nonparametric statistical analysis, respectively. $^{\#}P < 0.05$, $^{\#\#}P < 0.01$, $^{\#\#\#\#}P < 0.0001$ compared with WT group. $\hat{}\hat{}P < 0.01$, $\hat{}\hat{}\hat{}P < 0.001$, $\hat{}\hat{}\hat{}\hat{}P < 0.0001$ compared with vehicle group. $^{**}P < 0.01$, $^{***}P < 0.001$ compared with alglucosidase alfa group. After 2 additional administrations (12 total), tissues were collected 14 days after the last administration for histologic assessment (**C**–**E**). (**C**) Histogram showing the relative fiber size distribution frequency in quadriceps based on a bin size of 10 μm in Min FD. The Min FD values within each bin were greater than the lower limit and did not exceed the upper limit. The average distribution frequency for fibers with Min FD not exceeding 5 μm or larger than 85 μm was less than 0.1% and thus not included in the graph. Number of fibers analyzed per mouse is indicated in Supplemental Table 1. Error bars are SD. (**D**) Min FD across different groups. Individual values and mean ± SD are shown (n = 5–6 per group). ns, not significant. $^{*}P < 0.05$; $^{**}P < 0.01$; $^{****}P < 0.0001$ by Tukey's multiple comparison under 1-way ANOVA. For **C** and **D**, more than 20,000 fibers were analyzed for each of the treated

groups and more than 16,000 fibers for the WT (see also Supplemental Table 1). (**E**) Representative images of dysferlin-stained sections of muscle samples from quadriceps and triceps. *n* = 6–7 per group. Note that the extensive vacuolar change in all samples was the result of freezing artifact. Original magnification, ×200. Scale bars: 100 μm.

The reversal of increased phosphorylation of glycogen synthase (the protein is inactivated upon phosphorylation) to the WT level in ATB200/AT2221–treated *Gaa*-KO muscle suggests a shift in energy utilization. Our recent metabolite analysis of muscle from *Gaa*-KO mice indicates that the diseased muscles are utilizing fats and amino acids for energy rather than glucose (83). Interestingly, altered energy balance has been documented in several other lysosomal storage disorders irrespective of the storage material (84, 85).

A previously, to our knowledge, unreported finding is the mislocalization of dysferlin, a membrane protein, in the sarcoplasm of skeletal muscle fibers of *Gaa*-KO mice. In healthy individuals, dysferlin localizes to the sarcolemma in skeletal muscle (86). Abnormal dysferlin staining in the cytoplasm is frequently observed in patients with muscular dystrophies and in some patients with dysferlinopathy, suggesting that the phenomenon is a common feature of the myopathic process (87, 88). In fact, the clinical presentation of Pompe disease can resemble that of many musculoskeletal disorders, in particular, muscular dystrophies presenting with limb-girdle muscle weakness (59, 60, 89). The aberrant localization of dysferlin has been attributed to the damage of muscle membrane and/or to the disruption of proteins in the dysferlin complex (87, 88). The same may be true in Pompe muscles, thus adding yet another step to the complex pathogenic cascade leading to muscle damage. The reversal of abnormal dysferlin localization in *Gaa*-KO muscle by ATB200/AT2221, but not by alglucosidase alfa, provides additional evidence of the beneficial effects of ATB200/AT2221.

Thus, this head-to-head preclinical comparison of ATB200/AT2221 and alglucosidase alfa demonstrated that ATB200/AT2221 is more effective in glycogen reduction, alleviation of autophagic pathology, and improvement in muscle morphology and function in Pompe mice. Importantly, ATB200/AT2221 is currently being investigated as a next-generation therapy for Pompe patients (NCT02675465). The encouraging results from a phase 1/2 trial, combined with the results of extensive preclinical study, suggest that this investigational therapy has the potential to be a more effective treatment for this fatal disorder.

However, the questions that still need to be answered are whether the long-term ERT with ATB200/AT2221 would fully reverse the pathogenic cascade triggered by the lysosomal glycogen storage and if yes, at what stage of the disease progression. An additional consideration that should be taken into account is the need for targeting both skeletal muscle and the central nervous system (CNS) in patients with IOPD. The contribution of neurological deficits to the pathophysiology of the disease due to glycogen storage in the brain, the spinal cord, and in respiratory-related motoneurons has been reported in *Gaa*-KO mice (90–92) and in alglucosidase alfa–treated long-term IOPD survivors (93–95). The reversal of the CNS pathology may require additional remedy.

Methods

Antibodies

The following primary antibodies were used for immunoblotting: rabbit anti–human GAA polyclonal (custom antibody produced by Covance), rabbit anti–human GAA polyclonal antisera (FL-059, a gift from Barry Byrne, University of Florida, Gainesville, Florida, USA), mouse anti–human SQSTM1/p62 monoclonal (ab56416, Abcam), mouse anti–human Gapdh monoclonal (ab9484, Abcam or 39-8600, Invitrogen), rabbit anti–human GSK-3β monoclonal (9315, Cell Signaling Technology), rabbit anti–human phospho-GSK-3β (Ser9) monoclonal (9323, Cell Signaling Technology), rabbit anti–human glycogen synthase monoclonal (3886, Cell Signaling Technology), and rabbit anti–human phospho-glycogen synthase polyclonal (Ser641) (3891, Cell Signaling Technology). Rat anti–mouse Lamp1 monoclonal (553792, BD Biosciences), rabbit anti–human LC3B polyclonal (L7543, Sigma-Aldrich) mouse monoclonal anti-vinculin (clone hVIN-1; Sigma-Aldrich), and mouse monoclonal anti–α-tubulin (clone DM1A; Sigma-Aldrich) antibodies were used for immunostaining of single myofibers. Rabbit anti–human SQSTM1/p62 polyclonal (LS-B4617, LifeSpan BioSciences), rabbit anti–human LC3A monoclonal (4599, Cell Signaling Technology), mouse anti–human slow skeletal myosin heavy chain monoclonal (ab11083, Abcam), rabbit anti–mouse laminin polyclonal (ab11575, Abcam), and rabbit anti–human dysferlin monoclonal (ab124684, Abcam) were used for IHC. Horseradish peroxidase–conjugated (HRP-conjugated) goat anti-rabbit and goat anti-mouse secondary antibodies for Western blotting were purchased from Jackson ImmunoResearch. Secondary antibodies for IHC (rabbit-on-rodent HRP polymer

[RMR622] and mouse-on-mouse HRP polymer [MM620]) were purchased from Biocare Medical. Fluorescence-conjugated secondary antibodies were purchased from Invitrogen or LI-COR Biosciences.

In vitro thermostability assay

The stability of ATB200 was assessed with a modified fluorescence thermostability assay (96) using an Agilent Stratagene Mx3005P system (Eppendorf) in either neutral (50 mM sodium phosphate, 150 mM sodium chloride, pH 7.4) or acidic pH (50 mM sodium acetate, 150 mM sodium chloride, pH 5.2) buffer. Briefly, ATB200 (3.0 μg) was combined with SYPRO Orange and 0, 10, 30 or 100 μM AT2221 in a final reaction volume of 25 μl. A thermal gradient was applied to the plate at a rate of 1°C/minute, during which time the fluorescence of SYPRO Orange was continuously monitored. The fluorescence intensity at each temperature was normalized to the maximum fluorescence after complete thermal denaturation and analyzed by a Boltzman sigmoidal nonlinear regression to determine the melting temperatures.

Ex vivo stability assay

ATB200 (final concentration 3 μM) with or without AT2221 (final concentration 17 μM or 170 μM) was added to PBS (pH 7.4) or to a pool of fresh human blood from 10 individual donors; GAA activity was measured immediately, and after 2- and 4-hour incubation at 37°C. For the activity assay, each sample was diluted to 1 μg/ml of ATB200 in the buffer containing 100 mM sodium acetate, 100 mM NaCl, 1.0 mg/ml BSA, 0.02% Triton, and 0.02% sodium azide, pH 4.8. Twenty-five microliters of the diluted sample was incubated with 50 μl 1 mM 4-methylumbelliferyl α-D-glucopyranoside (4-MU-α-D-Glc) (Melford) in substrate buffer (100 nM sodium acetate, pH 4.8, 0.02% sodium azide) at 37°C for 30 minutes. Reactions were stopped by addition of 125 μl 1 M glycine, pH 10.5. Fluorescence was measured on a Spectramax M2e (Molecular Devices) using an excitation wavelength of 370 nm and an emission wavelength of 460 nm (with auto cutoff); the activity (nmol/ml/h) was calculated based on a 4MU standard curve using Softmax Pro 6.4 software. For each sample, GAA activity after 2- or 4-hour incubation was normalized to its own baseline to calculate the percentage of remaining activity.

Animal models, treatments, and GAA activity measurement in blood

Cynomolgus monkeys (n = 4 males and 4 females/group) were administered 100 mg/kg ATB200 via a 2-hour continuous i.v. infusion, either alone or 30 minutes after an oral administration of 175 mg/kg AT2221. Plasma samples were derived from blood collected at preinfusion, and at 1, 2, 3, 4, 6, 12, and 26 hours after the start of infusion.

Eight-week-old male Sprague-Dawley rats received a single tail vein i.v. bolus injection of 20 mg/kg alglucosidase alfa, 20 mg/kg ATB200 alone, or 20 mg/kg ATB200 with oral coadministration of 10 mg/kg of AT2221 30 minutes prior to i.v. injection (ATB200/AT2221). Plasma samples were derived from blood collected (via jugular vein cannula) at predose, 15 minutes, 30 minutes, and 1, 1.5, 2, 3, 4, 8, and 24 hours after administration.

Sex- and age-matched WT and *Gaa*-KO mice (a mouse model of Pompe disease; ref. 97) were used. Both strains are on a 129SVE background. Eight-week-old male *Gaa*-KO mice received a single tail vein i.v. bolus injection of 20 mg/kg alglucosidase alfa, 20 mg/kg ATB200 alone, or ATB200/AT2221 (20 mg/kg and 10mg/kg, respectively, see previous paragraph). Plasma samples were derived from blood collected (via mandibular vein) at predose, 10 minutes, 30 minutes, and 1.5, 3, 5, and 24 hours after administration.

For PK of ATB200, GAA activity was measured in plasma samples from monkeys, rats, and *Gaa*-KO mice as described previously (98). The PK parameters were calculated from GAA activity using GraphPad Prism 7. For half-life ($t_{1/2}$) calculation, early time points were used to fit a 1-phase decay model with $1/y^2$ weighting to derive an α-phase (distributive) half-life.

For efficacy studies, male *Gaa*-KO mice (at the ages of 14–22 weeks) received biweekly (every 2 weeks) tail vein i.v. bolus injections of either vehicle (25 mM sodium phosphate buffer containing 20 mg/ml mannitol, 0.5 mg/ml polysorbate 80, and 2.92 mg/ml sodium chloride, pH 6.0), 20 mg/kg alglucosidase alfa, or ATB200/AT2221 (see the second paragraph in this section). The number of injections ranged from 1 to 12. Starting from the second administration of either alglucosidase alfa or ATB200/AT2221, diphenhydramine was injected intraperitoneally at a dose of 10 mg/kg 15 minutes prior to administration to reduce anaphylaxis.

Tissue processing and analysis

For biochemical analyses, muscle tissues were snap-frozen and stored at –80°C. For histological analyses, tissues were embedded in optimal cutting temperature (OCT) for cryosectioning or fixed in Z-fix for paraffin embedding.

Measurement of glycogen levels in tissue. Tissue glycogen levels were measured as described previously (98) with slight modifications. Briefly, tissue samples were homogenized on ice in deionized H_2O and centrifuged at 10,000 *g* at 4°C for 10 minutes; the lysates were then denatured at 100°C for 10 minutes and centrifuged at 13,000 *g* at 4°C for 10 minutes. Supernatants were diluted 4- to 8-fold and incubated (40 μl) with or without amyloglucosidase (10 μl; 800 U/ml in 0.5 M sodium acetate, pH 5.0, made fresh) in a low-evaporation, transparent, 96-well plate for 1 hour at 50°C. The plates were then incubated at 100°C for 10 minutes to stop the reaction, followed by cooling at 4°C for 1 hour and incubation with Glucose Assay Reagent (200 μl; Sigma-Aldrich) at room temperature for 15 minutes. Absorbance at 340 nm was measured on a Spectramax M2e. The glycogen content was calculated based on the glycogen standard curve (ranging from 3.1 to 400 μg/ml) and normalized to the protein concentration.

Immunohistochemistry, fiber size analysis, Lamp1 IHC signal quantification, and PAS staining. IHC analysis of muscle samples was performed as previously described (99). Staining with Lamp1, LC3, p62, and slow myosin heavy chain were performed on paraffin sections; dysferlin staining was carried out on cryosections. Typically, 1 section per animal from a group of 5–8 mice each was examined.

For PAS staining, muscle tissues were fixed in 2% paraformaldehyde (PFA), 3% glutaraldehyde, 8% sucrose in PBS for 48 hours at 4°C followed by postfixation in neutral-buffered formalin containing 1% periodic acid for another 48 hours at 4°C. Samples were embedded in paraffin and the staining was carried out as described previously (98).

IHC and PAS images were captured using a DS-5Mc color camera on an Eclipse 90i upright microscope equipped with NIS-Elements software (Nikon).

For fiber size analysis, quadriceps were transected around the mid-belly region and embedded in OCT. Laminin antibody-stained sections, one from each animal, were scanned at Histowiz on an Aperio AT2 whole-slide scanner (Leica Biosystems). The morphometric analysis was conducted at CytoInformatics using their proprietary algorithms. Measurements of Min FD were extracted from individual fibers and exported to an Excel file for statistical analysis.

For Lamp1 IHC signal quantification, the areas enclosed by Lamp1 signal were measured using Image-Pro software and normalized to the total area of the fibers.

TEM and methylene blue staining. Muscle tissues were fixed in 2% PFA/3% glutaraldehyde/8% sucrose in 0.1 M sodium cacodylate buffer, pH 7.4 for 48 hours at 4°C. Subsequently, the samples were placed in 0.1 M sodium cacodylate buffer containing 1% periodic acid and 4% PFA for another 48 hours at 4°C and sent to the EM Core Lab at Robert Wood Johnson Medical School (Piscataway, New Jersey, USA) for further processing and embedding in Embed812 resin (Electron Microscopy Sciences). For TEM analysis, thin sections (90 nm) were stained with saturated solution of uranyl acetate and lead citrate. Images were captured with an AMT XR111 digital camera (Advanced Microscopy Techniques) at 80 kV on a Philips CM12 transmission electron microscope. For methylene blue staining, semithin sections (1 μm) were stained with 1% methylene blue for 30 seconds. Images were captured using a DS-5Mc color camera on an Eclipse 90i upright microscope (Nikon).

Immunostaining of single muscle fibers and SHG microscopy. Muscle fixation, isolation of single fibers, and immunostaining were described in detail in Raben et al. (100). Four *Gaa*-KO mice from each group (vehicle, alglucosidase alfa treated, ATB200/AT2221 treated, and WT) were used to obtain single muscle fibers for immunostaining. For each immunostaining and for confocal analysis, at least 25 fibers were isolated. The animals received 4 biweekly injections of the drugs starting at the age of 14 weeks. The white part of gastrocnemius muscle was used for the experiments.

SHG microscopy was performed as described previously (53). Images were collected on a Leica SP5 NLO confocal microscope with a 3-W Mai Tai HP Ti:Sapphire laser (Newport/Spectra-Physics). The excitation wavelength was 870 nm and a 40×, 1.25 NA oil immersion objective was used. The forward SHG signal was collected in the transmitted light detector after a 435/20 band-pass and a 680 short-pass filter (Chroma Technology). Images were acquired with Leica LASAF 2.3.1 software.

Western blot analysis. Muscle tissues were homogenized in RIPA buffer (PBS containing 1% NP40, 0.5% sodium deoxycholate, 0.1% SDS, and a protease/phosphatase inhibitor cocktail [5872, Cell Signaling Technology]). Samples were centrifuged at 16,000 *g* at 4°C for 15 minutes. Protein concen-

trations of the soluble fractions were measured using the Bio-Rad Protein Assay. Equal amounts of protein were run in SDS-PAGE gels (Invitrogen) followed by transfer onto nitrocellulose membranes (Invitrogen). Membranes were immunoblotted using the indicated antibodies. HRP-chemiluminescence was developed using SuperSignal West Pico PLUS Chemiluminescent substrate (ThermoFisher Scientific). Blots were scanned and quantified using a ChemiDoc XRS+ system (Bio-Rad). Alternatively, fluorescence-conjugated secondary antibodies were used, and the blots were developed using FluorChem Imager (ProteinSimple) or an infrared imager (LI-COR Biosciences).

Functional muscle strength tests. For the grip-strength test, an axial force transducer grip meter (Columbus Instruments) designed for mice was used. Each mouse was held by the base of the tail and lowered toward a trapeze (triangle bar) mounted to the grip meter. Mice were allowed to grasp the bar with both forepaws and were then pulled by the tail away from the rod in one fluid motion. The maximal lateral force exerted on the gauge was recorded. Each mouse was assessed with 3 consecutive trials in 1 day and the average value is reported.

For wire-hang test, individual mice were placed on a wire grid constructed of cage mesh. The grid was then inverted and placed approximately 60 cm above an open plastic cage with soft cushioning/bedding. The time that the mouse was able to hang on to the grid (latency to fall) was recorded with a maximal cutoff value at 2 minutes. Each mouse was tested once on 2 separate days and the average value is reported.

Statistics

Statistical significance was determined by using Tukey's multiple comparison under 1-way ANOVA or 2-sided *t* test (GraphPad Prism version 7.0). For Figures 4 and 7, statistical significance was determined by 2-tailed Student's *t* test.

Study approval

Animal care and experiments were conducted in accordance with Rutgers University IACUC–approved protocols.

Author contributions

SX, YL, ST, MCDV, RG, KJV, HVD, NR, and RK designed the study. RK coordinated the study. All authors performed experiments, and analyzed and interpreted the data. SX, YL, KJV, RK, and NR wrote the manuscript. All authors approved the final version of the manuscript for publication.

Acknowledgments

We wish to thank Rajesh Patel for the TEM work on muscle samples and Barry Byrne for the gift of the anti–human GAA antibody. We also wish to thank Johnson Matthey Inc. for manufacturing AT2221 used in the current research. ER was supported by the Intramural Research Program of the National Institute of Arthritis and Musculoskeletal and Skin Diseases of the NIH. JM, RP, and NR were supported by the Intramural Research Program of the National Heart, Lung and Blood Institute of the NIH.

Address correspondence to: Nina Raben, National Institutes of Health, Building 50, Room 3533, 50 South Drive, Bethesda, Maryland 20892-8018, USA. Phone: 301.827.1704; Email: rabenn@mail.nih.gov. Or to: Richie Khanna, Amicus Therapeutics, 1 Cedar Brook Drive, Cranbury, New Jersey 08512, USA. Phone: 609.662.2018; Email: rkhanna@amicusrx.com.

1. Hirschhorn R, Reuser AJJ. Glycogen storage disease type II: Acid alphaglucosidase (acid maltase) deficiency. In Scriver CR, et al, eds. *The Metabolic and Molecular Basis of Inherited Disease*. New York, NY: McGraw-Hill; 2001:3389–3420.
2. van der Ploeg AT, Reuser AJ. Pompe's disease. *Lancet*. 2008;372(9646):1342–1353.
3. van den Hout HM, et al. The natural course of infantile Pompe's disease: 20 original cases compared with 133 cases from the literature. *Pediatrics*. 2003;112(2):332–340.
4. Kishnani PS, et al. A retrospective, multinational, multicenter study on the natural history of infantile-onset Pompe disease. *J Pediatr*. 2006;148(5):671–676.
5. Reuser AJ, et al. Glycogenosis type II (acid maltase deficiency). *Muscle Nerve Suppl*. 1995;3:S61–S69.
6. Parenti G, Andria G. Pompe disease: from new views on pathophysiology to innovative therapeutic strategies. *Curr Pharm Biotechnol*. 2011;12(6):902–915.
7. Winkel LP, et al. Enzyme replacement therapy in late-onset Pompe's disease: a three-year follow-up. *Ann Neurol*. 2004;55(4):495–502.
8. Van den Hout JM, et al. Long-term intravenous treatment of Pompe disease with recombinant human alpha-glucosidase from

milk. *Pediatrics*. 2004;113(5):e448–e457.
9. Kishnani PS, et al. Chinese hamster ovary cell-derived recombinant human acid alpha-glucosidase in infantile-onset Pompe disease. *J Pediatr*. 2006;149(1):89–97.
10. Nicolino M, et al. Clinical outcomes after long-term treatment with alglucosidase alfa in infants and children with advanced Pompe disease. *Genet Med*. 2009;11(3):210–219.
11. Chien YH, et al. Pompe disease in infants: improving the prognosis by newborn screening and early treatment. *Pediatrics*. 2009;124(6):e1116–e1125.
12. Rossi M, et al. Long-term enzyme replacement therapy for pompe disease with recombinant human alpha-glucosidase derived from chinese hamster ovary cells. *J Child Neurol*. 2007;22(5):565–573.
13. van der Ploeg AT, et al. Open-label extension study following the Late-Onset Treatment Study (LOTS) of alglucosidase alfa. *Mol Genet Metab*. 2012;107(3):456–461.
14. Toscano A, Schoser B. Enzyme replacement therapy in late-onset Pompe disease: a systematic literature review. *J Neurol*. 2013;260(4):951–959.
15. Hahn A, et al. Outcome of patients with classical infantile pompe disease receiving enzyme replacement therapy in Germany. *JIMD Rep*. 2015;20:65–75.
16. Prater SN, et al. Skeletal muscle pathology of infantile Pompe disease during long-term enzyme replacement therapy. *Orphanet J Rare Dis*. 2013;8:90.
17. Schoser B, et al. Survival and long-term outcomes in late-onset Pompe disease following alglucosidase alfa treatment: a systematic review and meta-analysis. *J Neurol*. 2017;264(4):621–630.
18. Kohler L, Puertollano R, Raben N. Pompe disease: from basic science to therapy. *Neurotherapeutics*. 2018;15(4):928–942.
19. Case LE, Beckemeyer AA, Kishnani PS. Infantile Pompe disease on ERT: update on clinical presentation, musculoskeletal management, and exercise considerations. *Am J Med Genet C Semin Med Genet*. 2012;160C(1):69–79.
20. Peng SS, Hwu WL, Lee NC, Tsai FJ, Tsai WH, Chien YH. Slow, progressive myopathy in neonatally treated patients with infantile-onset Pompe disease: a muscle magnetic resonance imaging study. *Orphanet J Rare Dis*. 2016;11(1):63.
21. Raben N, Roberts A, Plotz PH. Role of autophagy in the pathogenesis of Pompe disease. *Acta Myol*. 2007;26(1):45–48.
22. Raben N, et al. Deconstructing Pompe disease by analyzing single muscle fibers: to see a world in a grain of sand. *Autophagy*. 2007;3(6):546–552.
23. Raben N, et al. Replacing acid alpha-glucosidase in Pompe disease: recombinant and transgenic enzymes are equipotent, but neither completely clears glycogen from type II muscle fibers. *Mol Ther*. 2005;11(1):48–56.
24. Raben N, et al. Differences in the predominance of lysosomal and autophagic pathologies between infants and adults with Pompe disease: implications for therapy. *Mol Genet Metab*. 2010;101(4):324–331.
25. Banugaria SG, et al. The impact of antibodies on clinical outcomes in diseases treated with therapeutic protein: lessons learned from infantile Pompe disease. *Genet Med*. 2011;13(8):729–736.
26. de Vries JM, et al. High antibody titer in an adult with Pompe disease affects treatment with alglucosidase alfa. *Mol Genet Metab*. 2010;101(4):338–345.
27. Patel TT, Banugaria SG, Case LE, Wenninger S, Schoser B, Kishnani PS. The impact of antibodies in late-onset Pompe disease: a case series and literature review. *Mol Genet Metab*. 2012;106(3):301–309.
28. de Vries JM, et al. Pompe disease in adulthood: effects of antibody formation on enzyme replacement therapy. *Genet Med*. 2017;19(1):90–97.
29. Wisselaar HA, Kroos MA, Hermans MM, van Beeumen J, Reuser AJ. Structural and functional changes of lysosomal acid alpha-glucosidase during intracellular transport and maturation. *J Biol Chem*. 1993;268(3):2223–2231.
30. Braulke T, Bonifacino JS. Sorting of lysosomal proteins. *Biochim Biophys Acta*. 2009;1793(4):605–614.
31. Wenk J, Hille A, von Figura K. Quantitation of Mr 46000 and Mr 300000 mannose 6-phosphate receptors in human cells and tissues. *Biochem Int*. 1991;23(4):723–731.
32. Zhu Y, et al. Carbohydrate-remodelled acid alpha-glucosidase with higher affinity for the cation-independent mannose 6-phosphate receptor demonstrates improved delivery to muscles of Pompe mice. *Biochem J*. 2005;389(Pt 3):619–628.
33. Zhu Y, et al. Glycoengineered acid alpha-glucosidase with improved efficacy at correcting the metabolic aberrations and motor function deficits in a mouse model of Pompe disease. *Mol Ther*. 2009;17(6):954–963.
34. Maga JA, et al. Glycosylation-independent lysosomal targeting of acid α-glucosidase enhances muscle glycogen clearance in pompe mice. *J Biol Chem*. 2013;288(3):1428–1438.
35. Tong PY, Kornfeld S. Ligand interactions of the cation-dependent mannose 6-phosphate receptor. Comparison with the cation-independent mannose 6-phosphate receptor. *J Biol Chem*. 1989;264(14):7970–7975.
36. Valenzano KJ, et al. Identification and characterization of pharmacological chaperones to correct enzyme deficiencies in lysosomal storage disorders. *Assay Drug Dev Technol*. 2011;9(3):213–235.
37. Parenti G, et al. A chaperone enhances blood α-glucosidase activity in Pompe disease patients treated with enzyme replacement therapy. *Mol Ther*. 2014;22(11):2004–2012.
38. Parenti G, Moracci M, Fecarotta S, Andria G. Pharmacological chaperone therapy for lysosomal storage diseases. *Future Med Chem*. 2014;6(9):1031–1045.
39. Porto C, et al. The pharmacological chaperone N-butyldeoxynojirimycin enhances enzyme replacement therapy in Pompe disease fibroblasts. *Mol Ther*. 2009;17(6):964–971.
40. Abian O, Alfonso P, Velazquez-Campoy A, Giraldo P, Pocovi M, Sancho J. Therapeutic strategies for Gaucher disease: miglustat (NB-DNJ) as a pharmacological chaperone for glucocerebrosidase and the different thermostability of velaglucerase alfa and imiglucerase. *Mol Pharm*. 2011;8(6):2390–2397.
41. Raben N, et al. Glycogen stored in skeletal but not in cardiac muscle in acid alpha-glucosidase mutant (Pompe) mice is highly resistant to transgene-encoded human enzyme. *Mol Ther*. 2002;6(5):601–608.
42. Bijvoet AG, et al. Recombinant human acid alpha-glucosidase: high level production in mouse milk, biochemical characteristics, correction of enzyme deficiency in GSDII KO mice. *Hum Mol Genet*. 1998;7(11):1815–1824.
43. Moreland RJ, et al. Lysosomal acid alpha-glucosidase consists of four different peptides processed from a single chain precursor.

J Biol Chem. 2005;280(8):6780–6791.
44. Raben N, et al. Enzyme replacement therapy in the mouse model of Pompe disease. *Mol Genet Metab*. 2003;80(1-2):159–169.
45. Fukuda T, et al. Autophagy and mistargeting of therapeutic enzyme in skeletal muscle in Pompe disease. *Mol Ther*. 2006;14(6):831–839.
46. Spampanato C, et al. Transcription factor EB (TFEB) is a new therapeutic target for Pompe disease. *EMBO Mol Med*. 2013;5(5):691–706.
47. Nascimbeni AC, Fanin M, Tasca E, Angelini C, Sandri M. Impaired autophagy affects acid α-glucosidase processing and enzyme replacement therapy efficacy in late-onset glycogen storage disease type II. *Neuropathol Appl Neurobiol*. 2015;41(5):672–675.
48. Pankiv S, et al. p62/SQSTM1 binds directly to Atg8/LC3 to facilitate degradation of ubiquitinated protein aggregates by autophagy. *J Biol Chem*. 2007;282(33):24131–24145.
49. Bjørkøy G, Lamark T, Pankiv S, Øvervatn A, Brech A, Johansen T. Monitoring autophagic degradation of p62/SQSTM1. *Meth Enzymol*. 2009;452:181–197.
50. Kabeya Y, et al. LC3, a mammalian homologue of yeast Apg8p, is localized in autophagosome membranes after processing. *EMBO J*. 2000;19(21):5720–5728.
51. Campagnola PJ, Loew LM. Second-harmonic imaging microscopy for visualizing biomolecular arrays in cells, tissues and organisms. *Nat Biotechnol*. 2003;21(11):1356–1360.
52. Plotnikov SV, Millard AC, Campagnola PJ, Mohler WA. Characterization of the myosin-based source for second-harmonic generation from muscle sarcomeres. *Biophys J*. 2006;90(2):693–703.
53. Ralston E, et al. Detection and imaging of non-contractile inclusions and sarcomeric anomalies in skeletal muscle by second harmonic generation combined with two-photon excited fluorescence. *J Struct Biol*. 2008;162(3):500–508.
54. Raben N, et al. Suppression of autophagy permits successful enzyme replacement therapy in a lysosomal storage disorder--murine Pompe disease. *Autophagy*. 2010;6(8):1078–1089.
55. Xu S, et al. Impaired organization and function of myofilaments in single muscle fibers from a mouse model of Pompe disease. *J Appl Physiol*. 2010;108(5):1383–1388.
56. Takikita S, et al. Fiber type conversion by PGC-1α activates lysosomal and autophagosomal biogenesis in both unaffected and Pompe skeletal muscle. *PLoS ONE*. 2010;5(12):e15239.
57. Fanin M, Nascimbeni AC, Angelini C. Muscle atrophy in limb girdle muscular dystrophy 2A: a morphometric and molecular study. *Neuropathol Appl Neurobiol*. 2013;39(7):762–771.
58. Miljkovic N, Lim JY, Miljkovic I, Frontera WR. Aging of skeletal muscle fibers. *Ann Rehabil Med*. 2015;39(2):155–162.
59. Preisler N, et al. Late-onset Pompe disease is prevalent in unclassified limb-girdle muscular dystrophies. *Mol Genet Metab*. 2013;110(3):287–289.
60. Gutiérrez-Rivas E, et al. Targeted screening for the detection of Pompe disease in patients with unclassified limb-girdle muscular dystrophy or asymptomatic hyperCKemia using dried blood: A Spanish cohort. *Neuromuscul Disord*. 2015;25(7):548–553.
61. Matsuda C, et al. The sarcolemmal proteins dysferlin and caveolin-3 interact in skeletal muscle. *Hum Mol Genet*. 2001;10(17):1761–1766.
62. Barresi R. From proteins to genes: immunoanalysis in the diagnosis of muscular dystrophies. *Skelet Muscle*. 2011;1(1):24.
63. Hornsey MA, Laval SH, Barresi R, Lochmüller H, Bushby K. Muscular dystrophy in dysferlin-deficient mouse models. *Neuromuscul Disord*. 2013;23(5):377–387.
64. Cárdenas AM, González-Jamett AM, Cea LA, Bevilacqua JA, Caviedes P. Dysferlin function in skeletal muscle: Possible pathological mechanisms and therapeutical targets in dysferlinopathies. *Exp Neurol*. 2016;283(Pt A):246–254.
65. Nemes A, et al. Increased aortic stiffness in glycogenosis type 2 (Pompe's disease). *Int J Cardiol*. 2007;120(1):138–141.
66. Goeber V, Banz Y, Kaeberich A, Carrel T. Huge aneurysm of the ascending aorta in a patient with adult-type Pompe's disease: histological findings mimicking fibrillinopathy. *Eur J Cardiothorac Surg*. 2013;43(1):193–195.
67. Wens SC, et al. Phenotypical variation within 22 families with Pompe disease. *Orphanet J Rare Dis*. 2013;8:182.
68. Zhang B, et al. Late-onset Pompe disease with complicated intracranial aneurysm: a Chinese case report. *Neuropsychiatr Dis Treat*. 2016;12:713–717.
69. Malhotra K, Carrington DC, Liebeskind DS. Restrictive arteriopathy in late-onset Pompe disease: Case report and review of the literature. *J Stroke Cerebrovasc Dis*. 2017;26(8):e172–e175.
70. McNamara ER, Austin S, Case L, Wiener JS, Peterson AC, Kishnani PS. Expanding our understanding of lower urinary tract symptoms and incontinence in adults with pompe disease. *JIMD Rep*. 2015;20:5–10.
71. Chan J, et al. The emerging phenotype of late-onset Pompe disease: A systematic literature review. *Mol Genet Metab*. 2017;120(3):163–172.
72. Fukuda T, et al. Dysfunction of endocytic and autophagic pathways in a lysosomal storage disease. *Ann Neurol*. 2006;59(4):700–708.
73. Koeberl DD, Li S, Dai J, Thurberg BL, Bali D, Kishnani PS. β2 Agonists enhance the efficacy of simultaneous enzyme replacement therapy in murine Pompe disease. *Mol Genet Metab*. 2012;105(2):221–227.
74. Koeberl DD, et al. Adjunctive albuterol enhances the response to enzyme replacement therapy in late-onset Pompe disease. *FASEB J*. 2014;28(5):2171–2176.
75. Lim JA, Li L, Raben N. Pompe disease: from pathophysiology to therapy and back again. *Front Aging Neurosci*. 2014;6:177.
76. He C, Klionsky DJ. Regulation mechanisms and signaling pathways of autophagy. *Annu Rev Genet*. 2009;43:67–93.
77. Drost MR, Hesselink RP, Oomens CW, van der Vusse GJ. Effects of non-contractile inclusions on mechanical performance of skeletal muscle. *J Biomech*. 2005;38(5):1035–1043.
78. Terman A, Brunk UT. Oxidative stress, accumulation of biological 'garbage', and aging. *Antioxid Redox Signal*. 2006;8(1-2):197–204.
79. Raben N, et al. Suppression of autophagy in skeletal muscle uncovers the accumulation of ubiquitinated proteins and their potential role in muscle damage in Pompe disease. *Hum Mol Genet*. 2008;17(24):3897–3908.
80. Lim JA, Li L, Shirihai OS, Trudeau KM, Puertollano R, Raben N. Modulation of mTOR signaling as a strategy for the treatment of Pompe disease. *EMBO Mol Med*. 2017;9(3):353–370.
81. Schiaffino S, Hanzlíková V. Autophagic degradation of glycogen in skeletal muscles of the newborn rat. *J Cell Biol*. 1972;52(1):41–51.

82. Kotoulas OB, Kalamidas SA, Kondomerkos DJ. Glycogen autophagy in glucose homeostasis. *Pathol Res Pract*. 2006;202(9):631–638.
83. Lim JA, Sun B, Puertollano R, Raben N. Therapeutic Benefit of Autophagy Modulation in Pompe Disease. *Mol Ther*. 2018;26(7):1783–1796.
84. Woloszynek JC, Kovacs A, Ohlemiller KK, Roberts M, Sands MS. Metabolic adaptations to interrupted glycosaminoglycan recycling. *J Biol Chem*. 2009;284(43):29684–29691.
85. Woloszynek JC, Coleman T, Semenkovich CF, Sands MS. Lysosomal dysfunction results in altered energy balance. *J Biol Chem*. 2007;282(49):35765–35771.
86. Piccolo F, Moore SA, Ford GC, Campbell KP. Intracellular accumulation and reduced sarcolemmal expression of dysferlin in limb--girdle muscular dystrophies. *Ann Neurol*. 2000;48(6):902–912.
87. Tagawa K, et al. Protein and gene analyses of dysferlinopathy in a large group of Japanese muscular dystrophy patients. *J Neurol Sci*. 2003;211(1–2):23–28.
88. Gallardo E, et al. Comparison of dysferlin expression in human skeletal muscle with that in monocytes for the diagnosis of dysferlin myopathy. *PLoS One*. 2011;6(12):e29061.
89. Hagemans ML, et al. Clinical manifestation and natural course of late-onset Pompe's disease in 54 Dutch patients. *Brain*. 2005;128(Pt 3):671–677.
90. Sidman RL, et al. Temporal neuropathologic and behavioral phenotype of 6neo/6neo Pompe disease mice. *J Neuropathol Exp Neurol*. 2008;67(8):803–818.
91. DeRuisseau LR, et al. Neural deficits contribute to respiratory insufficiency in Pompe disease. *Proc Natl Acad Sci USA*. 2009;106(23):9419–9424.
92. Turner SM, Hoyt AK, ElMallah MK, Falk DJ, Byrne BJ, Fuller DD. Neuropathology in respiratory-related motoneurons in young Pompe (Gaa(-/-)) mice. *Respir Physiol Neurobiol*. 2016;227:48–55.
93. Ebbink BJ, et al. Cognitive decline in classic infantile Pompe disease: An underacknowledged challenge. *Neurology*. 2016;86(13):1260–1261.
94. Ebbink BJ, et al. Classic infantile Pompe patients approaching adulthood: a cohort study on consequences for the brain. *Dev Med Child Neurol*. 2018;60(6):579–586.
95. McIntosh PT, et al. Neuroimaging findings in infantile Pompe patients treated with enzyme replacement therapy. *Mol Genet Metab*. 2018;123(2):85–91.
96. Niesen FH, Berglund H, Vedadi M. The use of differential scanning fluorimetry to detect ligand interactions that promote protein stability. *Nat Protoc*. 2007;2(9):2212–2221.
97. Raben N, et al. Targeted disruption of the acid alpha-glucosidase gene in mice causes an illness with critical features of both infantile and adult human glycogen storage disease type II. *J Biol Chem*. 1998;273(30):19086–19092.
98. Khanna R, et al. The pharmacological chaperone AT2220 increases recombinant human acid α-glucosidase uptake and glycogen reduction in a mouse model of Pompe disease. *PLoS One*. 2012;7(7):e40776.
99. Khanna R, et al. The pharmacological chaperone AT2220 increases the specific activity and lysosomal delivery of mutant acid alpha-glucosidase, and promotes glycogen reduction in a transgenic mouse model of Pompe disease. *PLoS One*. 2014;9(7):e102092.
100. Raben N, Shea L, Hill V, Plotz P. Monitoring autophagy in lysosomal storage disorders. *Meth Enzymol*. 2009;453:417–449.